Appendix for OPTIMAL PATH FOR ORBITAL DEBRIS

ANELÍ BONGERS
Department of Economics, University of Malaga, Spain

JOSÉ L. TORRES
Department of Economics, University of Malaga, Spain

This appendix is intended to provide more detail and additional information on the derivation and calibration of the different components of the DISE-2024 (Dynamic Integrated Space Economy) model. Although this is an economic paper, we have sought to balance the explanation of the different variables and parameters of the model for both economists and space engineers. This appendix is organized into eight sections: Basic data; Initial values for the base year; Calibration of economic parameters; Calibration of physical parameters; Exogenous sources of economic growth; Launch cost; The equations of the model; and Computer codes.

Anelí Bongers: abongers@uma.es
José L. Torres: jtorres@uma.es

APPENDIX A: BASIC DATA

DISE-2024 is a global, aggregate, dynamic integrated economy-space model (a type of Integrated Assessment Model, IAM) that encompasses both human activities in the Earth and outer space. Following the tradition of climate-change IAMs, the model consists of two interdependent modules: an economic module and a space environmental module. Human activity in space produces a negative externality in the form of orbital debris deteriorating the space environment, which in turn negatively affects economic growth. The economic module is based on the optimal neoclassical growth model by Ramsey (1928), which is extended to incorporate a space economy sector. The space environmental module is built on a three-equations dynamical system that models the accumulation of three types of orbital debris: derelict satellites, rocket bodies, and fragments. Given the diverse nature of variables and parameters in DISE-2024, we draw on a wide range of data sources, including economic databases from the World Bank, International Monetary Fund (IMF), Penn World Table (PWT), Bureau of Economic Analysis (BEA), and United Nations Population Division, as well as space activity databases from the National Aeronautics and Space Administration (NASA), European Space Agency (ESA), Union of Concerned Scientists, (UCS), Space-Track (US Space Forces), Satellite Industry Association (SIA), Space Foundation, and Jonathan C. McDowell databases.

Human activity in space began in 1957. Since then, space has been populated by an increasing number of human-made objects. A portion of these objects are operational satellites that provide a variety of services to Earth's users. However, another significant portion consists of non-functional objects, classified as orbital debris, which are by-products of launches, operational activities in orbit, and an endogenous in-orbit process of debris fragments emissions due to breakups and collisions. Regarding human activity in outer space, two key data points are fundamental: the number of launches and the number of satellites inserted into orbit, both of which are considered components of investment in the space sector.

The number of launches is a fundamental variable in the analysis for three reasons. First, launches are the current technical method by which spacecraft are inserted into orbit. While not an economic variable in themselves, launches are an integral part of the investment process in space capital. Second, the number of satellites per launch varies depending on the launch vehicle and the size of the satellites, which decouples rocket launches from the number of satellites inserted into orbit. Third, launches are the primary source of orbital debris with the current technology. Most existing launch vehicles consist of several stages, and the upper stages of rocket bodies often remain in orbit after the payload has been deployed. Additionally, during the payload insertion phase, various pieces (such as payload fairings and connection parts between stages) are jettisoned.

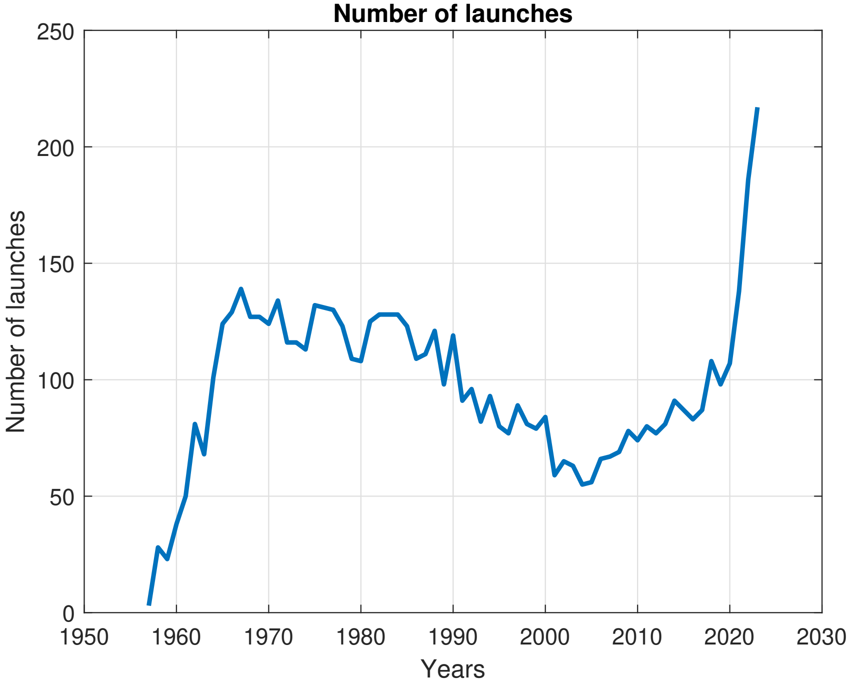

FIGURE A.1. Number of launches per year (1957-2023). Source: NASA

Figure A.1 plots the annual number of launches for the period 1957-2023. Over time, we can distinguish four stages. The first stage covers the first 10 years of space exploration, during which the number of launches increases rapidly, primarily driven by the space-race between the US and the Soviet Union. From the early 1970s to the end of the century, we observe a decline in the number of launches, as the space-race between the two superpowers lost intensity, and also due to the disintegration of the Soviet Union. The third stage begins with the new century and the entry of private firms into the market, firms that are not only satellite operators, but with launch capabilities (the new space economy). This state spans from 2000 to 2021. In 2022 launch activity experimented a sharp increase with the advent of satellite constellations, and in particular, with the activation of the Starlink satellite constellation by SpaceX, the leading and most active space firm on the World. The number of launches in 2020 was 107, but increased to 138 in 2021, 186 in 2022, and 217 in 2023.

Figure A.2 displays the number of new satellites inserted into orbit each year. A significant change is clearly visible in the last three years of the sample period. For most of the period, the number of new satellites inserted into orbit remained relatively constant, at around 200 per year. However, this trend began to shift in 2014 with the entry of more private firms into the market, and particularly accelerated in 2022 and 2023 with the launch of large satellite constellations. Although 542 satellites were inserted into orbit in 2019, this number increased to 2,950 by 2023. The large number of satellites inserted in the last two years is mainly due to the deployment of Starlink satellite constellation of SpaceX and the OneWeb satellite constellation.

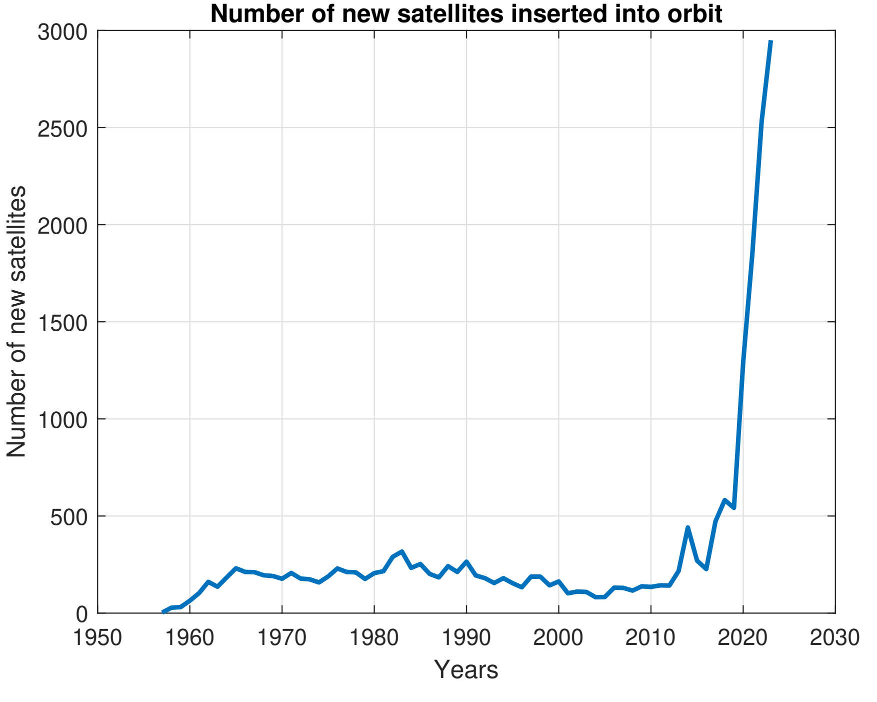

FIGURE A.2. Number of new satellites inserted into orbit (1957-2023). Source: NASA

Table A.1 shows some relevant data about human activity in Earth's orbits and the amount of debris estimated by the ESA as of December 2023. Since the beginning of space exploration until December 2023, around 6,500 successful launches have taken place. The total number of satellites launched is 16,990, although only 11,500 remains in Earth' orbit. Of this number, around 8,500 to 9,000 are operational. As already indicated, a rocket launch can include more than one satellite or spacecraft. Indeed, the relationship between launches and new satellites in orbit is changed dramatically in recent years due to the use of small and micro satellites and the higher power and payload capacity of launch systems. The number of estimated incidents by the ESA, including break-ups, explosions, collisions, or anomalous events, resulting in fragmentation, is approximately 630. The NASA Breakups database by Anz-Meador et al. (2022) identifies a total of 268 breakup events, including collisions of intact objects with debris, deliberate collisions, self-destruction of payloads, and explosions of intact objects. One of the most significant incidents was the collision on February 10, 2009 between an active US communications satellite (*Iridium 33*) with a defunct Russian military communications satellite (*Kosmos 2251*). Both satellites were destroyed in the collision, producing around 2,200 pieces of new tracked debris measuring at least 5 cm (NASA, 2007). However, the most severe incident was intentional: an anti-satellite military test that resulted in the destruction of the *Fengyun-1C* (a Chinese satellite) on January 1, 2011, by a kinetic weapon, producing an estimated 3,037 pieces of new tracked debris (NASA,2011). Most of the activity takes place at Low-Earth-Orbit (LEO, between 200 and 2,000 km), and at Geostationary Orbit (GEO, at 35,786 km).

The categorization of space debris is typically based on size and the availability of appropriate technology for tracking fragments in outer space. Orbital debris is tracked using Earth-based radar systems and optical telescopes. These systems can detect and monitor objects larger than 10 cm in low Earth orbit (LEO) and larger than 30 cm in geostationary orbit (GEO). In general, debris are classified according to size into three categories: Debris larger than 10 cm, debris between 1 cm and 10 cm, and debris between 1 mm and 1 cm. This classification is also based on the expected damage that can be produced by a piece of debris depending on its size. The NASA Standard Breakup model (Johnson et al., 2001) estimates that a catastrophic collision occurs when the ratio of the impactor energy to mass of the target exceeds 40 Joules (J) per gram (g). Locke et al. (2024) define a catastrophic collision as one in which two objects collide at an impact velocity above 6 kilometers (km) per second (s) and with an energy in the range 35-45 J/g, sufficient for both to break apart. For a collision speed of 10 km/s of a 10 cm impactor, Locke et al. (2024) estimate a lower bound of an impact energy of 1.3 MJ, or about 9 J/g for a large satellite and 59 J/g for a small satellite. These authors assume that the probability of a catastrophic event is 100% for a debris of 10 cm, 10% for a debris of 1 cm, and 0.01% for a debris of 1 mm. They use a simple probabilistic model using previous figures, resulting in an average lethality probability of 21.7% for debris between 1 cm and 10 cm, and an average lethality probability of 0.09% for debris between 1 mm and 1 cm. A 3 mm of debris impacting at 10 km/s produces an energy similar to a bullet (a kinetic energy of 1.9 KJ, equivalent to 0.45 grams of TNT), and a 1 cm piece produces a kinetic energy of 70.7 KJ (equivalent to 16 grams of TNT). McKnight et al. (2021) indicate that, using data from growth test and on-orbit tests, the energy threshold for catastrophic breakups is 40 J/g of target mass. This corresponds to a target mass to projectile mass ratio of 1250 at 10 km/s (Kessler et al., 2010). Breakups models consider that fragments larger than 20 cm typically have a mass of over 1 kg and would almost always cause a catastrophic collision. The LEGEND model predicts that only 45% of the collision between cataloged objects (those larger than 10 cm) will be catastrophic, and 55% will be non-catastrophic (Johnson et al., 2001).

TABLE A.1. Basic space data

Number of rocket launches	6,500
Number of satellites inserted into orbit	16,990
Number of satellites in orbit	11,500
Number of operational satellites	9,000
Number of fragmentation events ESA	630
Number of fragmentation events NASA	268
Number of rocket bodies	2,050
Number of derelict satellites	3,500
Number of tracked objects by SSN	35,150
Estimated number of orbital debris greater than 10cm	36,500
Estimated number of orbital debris between 1cm and 10cm	1,000,000
Estimated number of orbital debris between 1mm and 1cm	130,000,000

Source: ESA and NASA. December 2023.

Based on previous information, we can conclude that debris smaller than 1 cm generally poses a low risk of catastrophic satellite damage. While their destructive power is estimated to be minimal, such debris can still significantly impair critical systems and shorten the operational lifespan of satellites. On the other hand, debris larger than 1 cm can be very dangerous due to the high speed of collisions. Therefore, in calculations the probability of destruction for operational satellites, derelict satellites, and rocket bodies, we use the population of debris larger than 1 cm.

Projections from various space debris models, such as ESA's MASTER (Meteoroid and Space Debris Terrestrial Environment Reference) model, estimate that as of December 2023, there are 36,500 pieces of debris larger than 10 cm in diameter, 1,000,000 objects between 1 cm and 10 cm, and over 130 million fragments between 1 mm and 1 cm. As os that date, the total number of debris pieces tracked by the United States Space Surveillance Network (SSN) was 35,150.

For calibration and computational reasons (particularly due to variable scaling), we first calculate the population of orbital debris larger than 10 cm, which we assume can be approximated by the number of tracked and cataloged non-operational objects. Then, using estimates from the ESA's MASTER model, we calculate the ratio between the estimated number of debris between 1 cm and 10 cm and the estimated number of debris larger than 10 cm to obtain the total number of debris larger than 1 cm, which are considered potentially fatal.

A.1 *Operational satellites*

Using the model's equations and historical data, we estimate key space variables, namely the number of operational satellites in orbit and the number of satellites destroyed by collisions. First, the stock of operational satellites in orbit is estimated using the following equation for t=1957 to 2023,

$$S_t = (1 - \delta_s)S_{t-1} + H_t - X_t \tag{A.1}$$

where S_t is the stock of satellites at time t, H_t is the number of newly inserted satellites as shown by Figure A.2, X_t is the number of satellites destroyed by collision with debris, and δ_s is the depreciation rate for satellites (see Appendix C). The initial value for the stock of satellites is $S_{1957} = 3$, given that $S_{1956} = 0$ and $H_{1957} = 3$. Figure A.3 plots the estimated stock of operational satellites for the period 1957 to 2023, resulting from running equation (A.1) for the period. Whereas the number of operational satellites were around 1,000 from 1970 to 2013, from 2016 onwards, the number of satellites experienced a sharp increase, with the building of Starlink and OneWeb satellite constellations. The estimated number of operational satellites for the year 2023 is of 8,391. The ESA estimates around 9,000 operational satellites. Those figures can be compared with the number of operational satellites in the USC satellite database at May 2023 (last update) of 7,561. Based on this information, we consider that the initial stock of satellites in orbit for the simulation of the model is of 8,500. Around 84% of operational satellites are in LEO, 12% in GEO, and the rest (4%) in MEO. However, the model is an aggregate model and does not distinguish by altitude.

Notice that, to compute the number of operational satellites in orbit, we need to know the number of satellites that have been destroyed by collision with orbital debris. The number of satellites destroyed is calculated as,

$$X_t = (1 - v_t)\theta D_t S_t \tag{A.2}$$

where D_t is the stock of orbital debris, v_t is the collision avoidance capability, and θ is the collision risk parameter (see Appendix D). In this expression, D_t represents pieces of debris larger than 1 cm. v_t represents the fraction of potential collisions that can be avoided by altering the orbit of the operational satellite. This depends on the tracking, alert-systems, and maneuvering capacities of the satellite. This variable will be a key factor for computing damages, and it represents a factor that disentangles the population of orbital debris with the risk of collision. In the baseline model, v_t takes a value of one for the collision avoidance and ESA zero debris scenarios, and a value of zero for the rest. This assumption

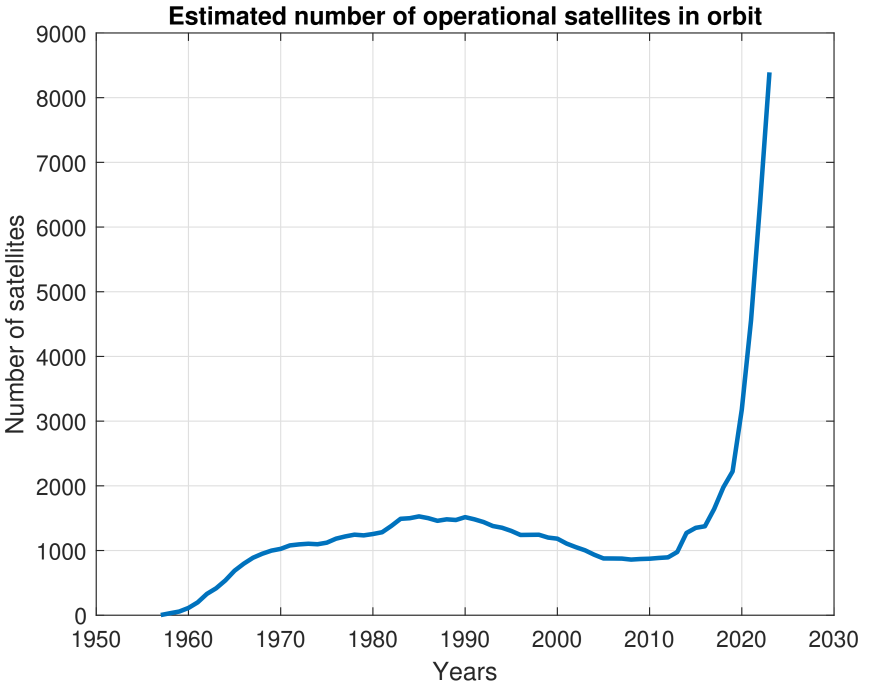

FIGURE A.3. Estimated stock of operational satellites (1957-2023)

is made for the sake of simplicity. In reality, the value of v_t is positive and increasing over time as tracking systems are developed and new satellites incorporate automatic collision avoidance systems.

Figure A.4 plots the estimated annual number of operational satellites destroyed by collisions resulting from the model for the period 1957-2023. The estimated number of fatal collisions is below 1, except for the last year of the sample period. Nevertheless, the accumulative sum of the estimation is seven for the full sample period. Estimated figures are not far from the data about losses of operational satellites by collision. Both the ESA's DISCOS database and the NASA's breakups database (Anz-Meador et al., 2022) account for a total of five collision events between operational satellites and orbital debris in each database. However, combining the two databases accounts for six different events and also includes a number of fragmentation events involving satellites for which the cause is unknown.

Many satellites have been lost or have suffered damages from impacts with micrometeorids and orbital debris, but also due to internal failures. Some of these events are only suspected, and difficult to determine the real cause of the damages. The earliest suspected

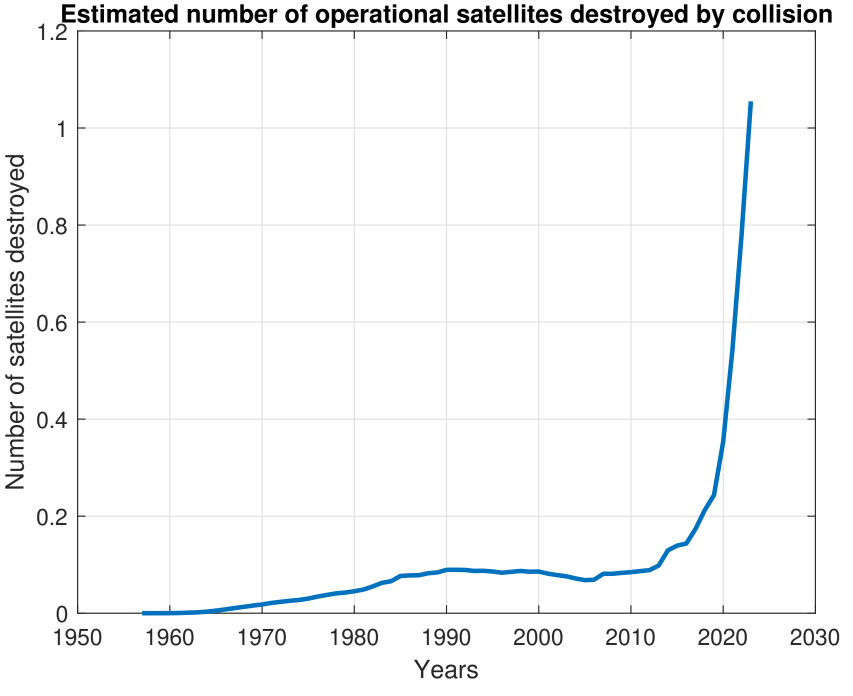

FIGURE A.4. Estimated number of operational satellites destroyed by collision

loss was of *Kosmos-1275*, a Soviet Union positioning satellite that fragmented on 24 July 1981 (a month after launch). However, there is no evidence that the destruction of this satellite was caused by a collision with orbital debris or by an internal explosion. NASA (2022) indicates that the Russian authorities reported that the destruction of the satellite was due to a battery explosion. Tracking by NASA showed that it broke up into 479 objects. The first known collision took place on December 23, 1991 with the destruction of *Cosmos-1934*. However, the ESA's DISCOS database classifies the fail of the *Ayame-1* due to the Delta rocket fails in the insertion into planned orbit on February 6, 1979, as a collision, given that the 3rd stage of the launcher came in contact with the satellite after separation, producing 3 cataloged debris. Another collision took placed on July 24, 1996, between a French microsatellite (*Cerise*) and debris from a French *Ariane-1 H-10* upper-stage rocket that had exploded in November 1986, but although the impact occurred, the satellite remained operational. The most significant known incident was the collision on February 10, 2009, between an active U.S. communications satellite (*Iridium-33*) and a defunct Russian military communications satellite (*Kosmos-2251*), resulting in the destruction of both satellites. This collision created around 2,370 pieces of catalogued pieces of debris. On August 23, 2016, the *Sentinel-1A* was hit by a small fragments on its sollar array, producing 9 cataloged debris. Finally, on November 21, 2021, the Yunhai-1-02 collided with a fragment of a Russian rocket, producing 37-38 fragments.

Table A.2 collects relevant information about operational satellite collision events as collected in the ESA's DISCOS database and in the NASA' Breakups databse by Anz-Meador et al. (2022).

TABLE A.2. Operational satellite collisions

Name	Date	Cataloged debris		Apogee (Km)	Perigee (Km)
		NASA	ESA		
Ayame-1	6-Feb-1979	–	3	–	–
Cosmos-1934	23-Dec-1991	3	2	1,010	950
Cerise	24-Jul-1996	2	1	675	665
Iridium-33	10-Feb-2009	2,371	2,375	780	775
Sentinel-1A	23-Aug-2016	9	–	698	696
Yunhai-1-02	15-Nov-2021	38	37	785	780

Source: ESA's DISCOS and NASA's Breakups (Anz-Meador et al., 2022).

Apart from the confirmed events included in ESA and NASA databases, there are more suspected but nonconfirmed colissions. On March 29, 2006, the Russian *Ekspress-AM11* communications satellite was struck by an unknown object and rendered inoperable. On March 12, 2010, *Aura* lost power from one-half of one of its 11 solar panels, which resulted damaged. On January 22, 2013, *BLITS* (a Russian laser-ranging satellite) was struck by debris suspected to be from the 2007 Chinese anti-satellite missile test, changing both its orbit and rotation rate. On 22 May 2013, *GOES-13* was hit by an object, which caused it to temporary lose track of the stars that it used to maintain an operational attitude.

A.2 *Orbital debris*

The stock of debris is calculated as the sum of three components: Intact objects comprising both derelict satellites and rocket bodies, and fragments. Following standard classification by ESA, fragments are defined depending on their size, considering three types: fragments larger than 10 cm, between 1 cm and 10 cm, and between 1mm and 1cm. We denote $F_{1,t}$ as the population of fragments larger than 10 cm, $F_{2,t}$ as fragments larger than 1 cm, and $F_{3,t}$ as fragments larger than 1mm. Derelict satellites and upper stages rocket bodies, including ullage motor, have sizes larger than 10 cm.

The amount of orbital debris is defined as,

$$D_{i,t} = W_t + Z_t + F_{i,t} \qquad \text{for} \qquad i = 1,2,3 \tag{A.3}$$

where W_t is the stock of derelict satellites, Z_t is the stock of rocket bodies, and $F_{i,t}$ is the stock of fragments other than derelict satellites and rocket bodies, depending on their size. In our analysis, the population of debris used to calculate the risk of collision is $D_{2,t}$, that is, debris larger than 1 cm in size. The model computes fragments larger than 10 cm. Then, we assume that,

$$F_{2,t} = (1 + \Gamma)F_{1,t} \tag{A.4}$$

where Γ is a scale parameter calibrated from the estimated population of debris fragments by size by the ESA (Appendix D).

In the space engineering literature, we can find a large number of orbital debris evolutionary models. In practice, several models for simulating the population dynamics of orbital debris have been developed by several authors (Farinella and Cordelli, 1991; Talent, 1992; Cordelli et al. 1993; Rossi et al. 1994; Rossi and Farinella, 1998; Lewis et al. 2009; Lafleur, 2011; Percy, 2015; Letizia et al. 2017, D'Ambrosio et al. 2022; and Lifson et al. 2022). On the other hand, debris evolutionary models have been developed by some governmental space agencies: the National Aeronautics and Space Administration (NASA), with the EVOLVE and LEGEND models; the European Space Agency (ESA), with the DELTA and MASTER models; the Japan Aerospace Exploration Agency (JAXA), with the NEODEEM model; the China National Space Administration (CNSA), with the SOLEM model; the United Kingdom Space Agency (UKSA), with the DAMAGE model, and the Centre National d'Estudes Spatiales (CNES), with the MEDEE model.

Farinella and Cordelli (1991) developed a simple model with two differential equations. Talent (1992) developed the PIB (particles-in-a-box) model. Lewis et al. (2009) developed the FADE (Fast Debris Evolution) model, consisting in a first-order differential equation to estimated the number of new objects larger than 10 cm that are added and removed from the environment. Lafleur (2011) extended the model by Farinella and Cordelli (1991) to include collisions between intact satellites (both operational or not) and between fragments. D'Ambrosio et al. (2022) and Lifson et al. (2022) develop a debris evolutionary model for LEO with the aim of obtaining an estimate on the maximum number of satellites can be fit in LEO. They used a PIB model based on a system of differential equations to describe the time evolution of different types of objects.

A variety of debris evolutionary models have been developed to integrate with economic models. Rouillon (2020) and Guyot and Ruillon (2023) developed a simplified model with two types of debris: large objects representing derelict satellites and rocket bodies, and small fragments. Rao and Letizia (2022) utilized a multi-shell and multi-species PIB model of the debris environment. Rao et al. (2023) developed the OPUS model. Percy (2015) and Guyot (2024) extended the two-population debris model to different layers (altitude), where atmospheric drag moves debris from upper layers to lower layers. Bongers and Torres (2023) developed a single dynamic equation with emissions related to launches and collisions. A more complex model was developed by Bongers et al. (2025).

The DAMAGE (Debris Analysis and Monitoring Architecture for the Geosynchronous Environment) model was developed by the University of Southampton (Lewis, 2020) for the UKSA. NASA developed initially the EVOLVE model in 1986 for LEO debris environment between 200 and 2000 km altitude (Krisko et al., 2001). The EVOLVE debris model has been replaced by the LEGEND (LEO-to-GEO Environmental Debris) model (Liou et al., 2004), which reproduces the historical debris environment from LEO to GEO. The ESA has developed the MASTER (Meteoroid and Space Debris Terrestrial Environment Reference) model as a replecement for the previous DELTA model, whereas the Japan Aerospace Exploration Agency (JAXA) developed the NEODEEM (Near Earth Orbital Debris Environment Evolutionary Model) model, and the China National Space Administration (CNSA) developed the SOLEM (Space Objects Long-term Evolution Model) model (Wang and Liu, 2019).

A.3 *Derelict satellites*

The first type of debris is abandoned end-life satellites in orbit. This is an intact object, but the presence of residual fuels and batteries can produce an explosion and fragmentation of these objects. The law of motion of derelict satellites, W_t, is given by,

$$W_{t+1} = (1 - \delta_w - \varepsilon_w)W_t - \theta(Z_t + F_{2,t} + (1 - v_t)S_t)W_t - \theta\frac{W_t^2}{2} + \chi\delta_s S_t \tag{A.5}$$

where δ_w is the natural orbital decay rate of derelict satellites, ε_w is the decay rate of derelict satellites due to breakups, v_t is the collision avoidance capability, and χ is the fraction of non-operational satellites abandoned in orbit. Values for these parameters can be found in Appendix D. The first term of the right side accounts for the reduction in the stock of derelict satellites due to natural causes or internal explosions. The second term of the right side accounts for the reduction due to collision with other debris and with operational satellites. Finally, the last term of the right side accounts for the number of non-operational satellites abandoned each period.

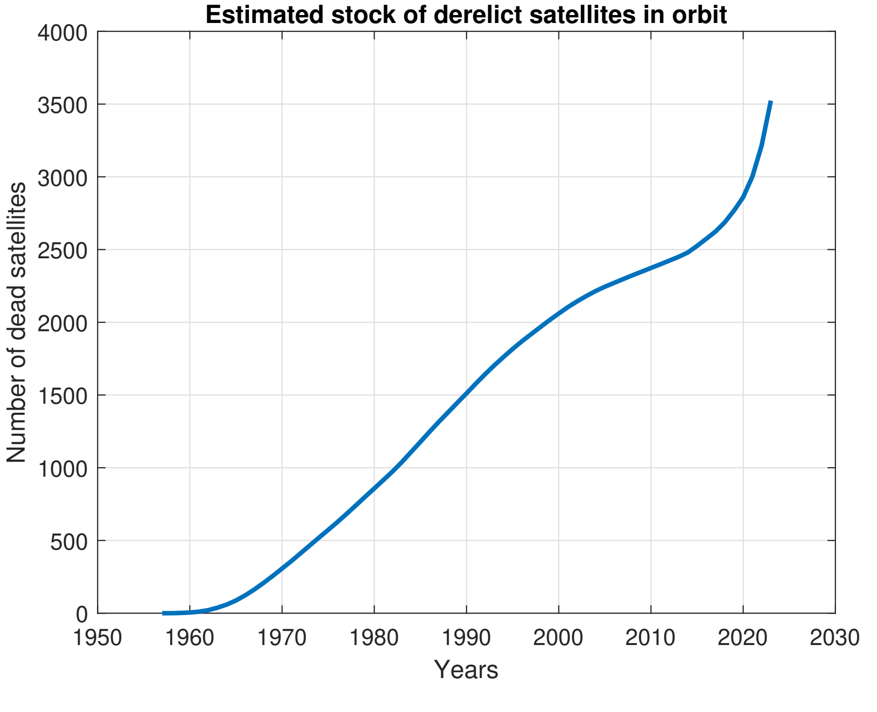

FIGURE A.5. Estimated number of derelict satellites (1957-2023)

This accumulation equation is used to estimate the stock of derelict satellites in orbit. The initial value for derelict satellites is set to zero. Accordingly to the ESA, the number of derelict satellites in orbit as of 2023 is approximately 3,000. The DISCOS database, as January 2025, reports a total of 13,582 payloads, encompassing both operational and non-operational satellites. Figure A.5 plots the estimated number of derelict satellites in orbit from the model for the period 1967-2023, with an estimated value of 3,524 for the year 2023.

Furthermore, it is possible compare the estimations with NASA's, estimates for the stock of spacecraft, which includes both operational satellites and derelict satellites (NASA, 2024). Figure A.6 compares the values from the NASA database with the sum of estimates values from Figures A.3 and A.5. For the period 1960 to 2010, the model's estimates are higher than the number of spacecraft tracked by NASA. However, the figures converge towards at the end of the period, which is significant as this will be the initial value used for the model simulation. In 2023, the NASA tracked 11,860 spacecraft, whereas the model estimates 11,915.

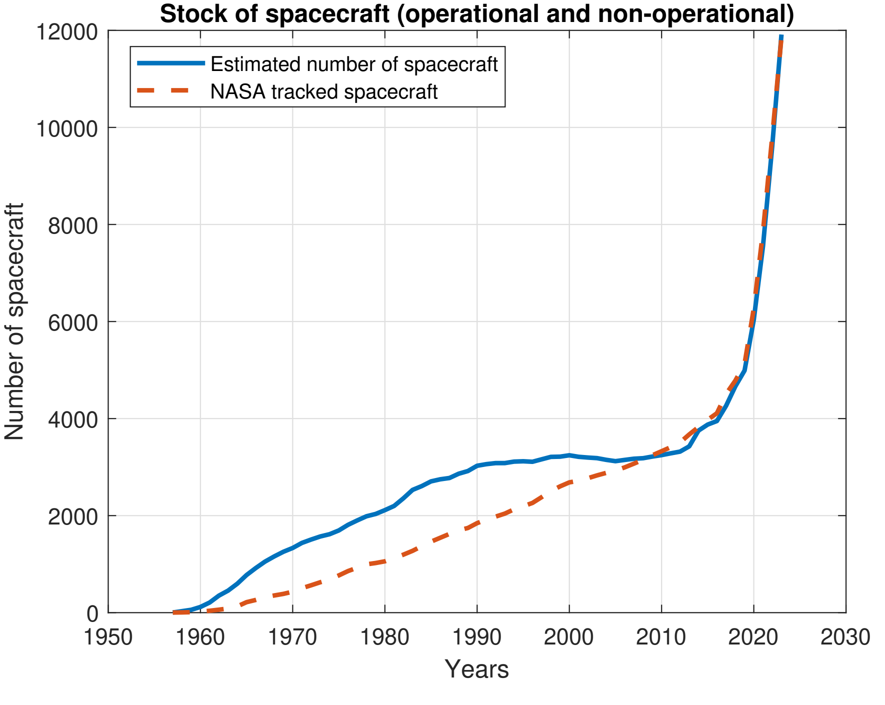

FIGURE A.6. Estimated number of spacecraft (1957-2023)

A.4 *Rocket bodies*

The second type of orbital debris is rocket bodies. Rocket bodies are the upper states of launch vehicle systems. Standard launch vehicles systems are composed of different stages (two to four). Whereas first stages are expended at low altitude and return to Earth, the last stage usually remains in orbit once the payload has been released if not deorbiting procedure is implemented.

As in the case of derelict satellites, rocket bodies are large intact objects that are susceptible to breakup. The final stages of launch system contain residual fuel and pressurized tanks that degrade under the extreme conditions of space, potentially leading to explosion and fragmentation of the rocket. According to Anz-Meador et al. (2022), there have been 83 rocket body breakups, resulting in a total of 8,315 tracked fragments. The first rocket body breakup occurred on 17 October 1970 with the explosion of a NASA *AGENA-D* stage. Additionally, ullage motors, relatively small rocket engines attached to the last stage of the launch system, are also intact objects subject to breakup. Anz-Meador et al. (2022) report 53 breakup events of ullage motors producing a total of 664 pieces of tracked debris.

Historically, not all final stages of launch vehicle systems have been abandoned into orbit, as some launch systems are reusable vehicles. This is exemplified by NASA's Space Shuttle program, which commenced its first flight in April 1981. The Space Shuttle was attached to a large external tank containing liquid oxygen and hydrogen, along with two solid rocket boosters (SRBs). In the first stage of flight, once the solid propellant was exhausted, the two SRBs were jettisoned and parachuted into the ocean for recovery and reuse. In the second stage, after the main engines consumed the propellants, the external tank was jettisoned, disintegrated upon reentry, and its remnants fell into the ocean. Payloads, such as satellites or other spacecraft, were deployed into orbit using a robotic arm. Upon mission completion, the orbiter vehicle re-entered Earth's atmosphere and landed for refurbishment and reuse. NASA's Space Shuttles completed 135 missions, whereas the Soviet Union's Buran shuttle completed only one flight. This type of launch vehicles can be classified as debris-free partially reusable launch vehicles. More recently, several private firms are developing reusable launch vehicles. SpaceX's Starship, although not yet operational, has completed four orbital test flights. The upcoming ninth test flight, scheduled for May 27, 2025, will mark the first time a previously flown Super Heavy booster is reused. This test is significant in advancing the development of fully reusable launch systems.

The accumulation equation of rocket bodies is a positive function of the number of launches, and a negative function of the natural decay rate, the breakups, and the collisions with debris. The law of motion for rocket bodies, Z_t, is given by,

$$Z_{t+1} = (1 - \delta_z - \varepsilon_z)Z_t - \theta(W_t + F_{2,t} + (1 - v_t)S_t)Z_t - \theta\frac{Z_t^2}{2} + \varphi L_t \tag{A.6}$$

whereas δ_z represents the natural decay rate of rocket bodies, ε_z denotes the fraction of rocket body breakups, φ is the fraction of rocket bodies per launch, and L_t is the number of launches at the time t. Tracked rocket bodies are included in the NASA database, Monthly objects in orbit by type.

Figure A.7 illustrates the trajectory of rocket bodies tracked by NASA along the estimates generated by the model using expression (A.6). Despite the approximation of constant parameters for natural decay and breakup rates of rocket bodies, the estimate resulting from expression (A.6) is similarly align the rocked bodies tracked by NASA.

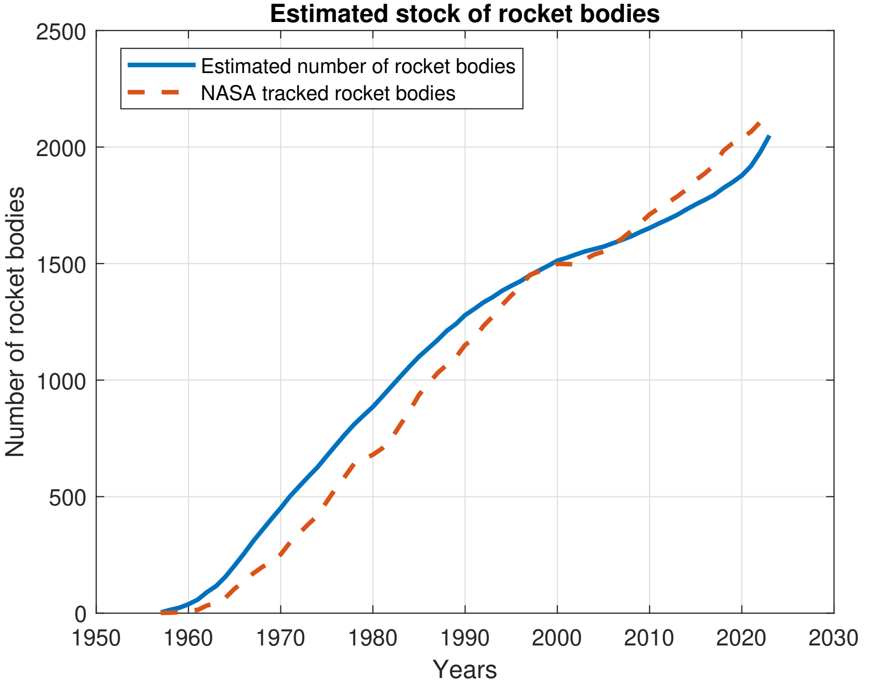

FIGURE A.7. Estimated number of rocket bodies and rocket bodies tracked by NASA

A.5 *Fragments*

Finally, the third type of debris is fragments. The law of motion for fragments includes two endogenous sources of orbital debris: Breakups and collisions. Formally,

$$F_{1,t+1} = (1-\delta_f)F_{1,t} + \omega L_t + \phi_w \varepsilon_w W_t + \phi_z \varepsilon_z Z_t + \gamma_s X_t + \gamma_w \theta (Z_t + F_{2,t}) W_t$$
$$+ \gamma_w \theta \frac{W_t^2}{2} + \gamma_z \theta (W_t + F_{2,t}) Z_t + \gamma_z \theta \frac{Z_t^2}{2} \qquad \text{(A.7)}$$

where δ_f denotes the natural decay rate of fragments, ω represents the number of fragments generated per launch, ϕ_w is the number of fragment produced per derelict satellite breakup, ϕ_z is the number of fragments per rocket body breakup, γ_s is the number of fragments resulting from a collision between an operational satellite and debris, γ_w is the number of fragments from a collision between derelict satellites with debris, and γ_z is the number of fragments resulting from a collision of rocket bodies with debris.

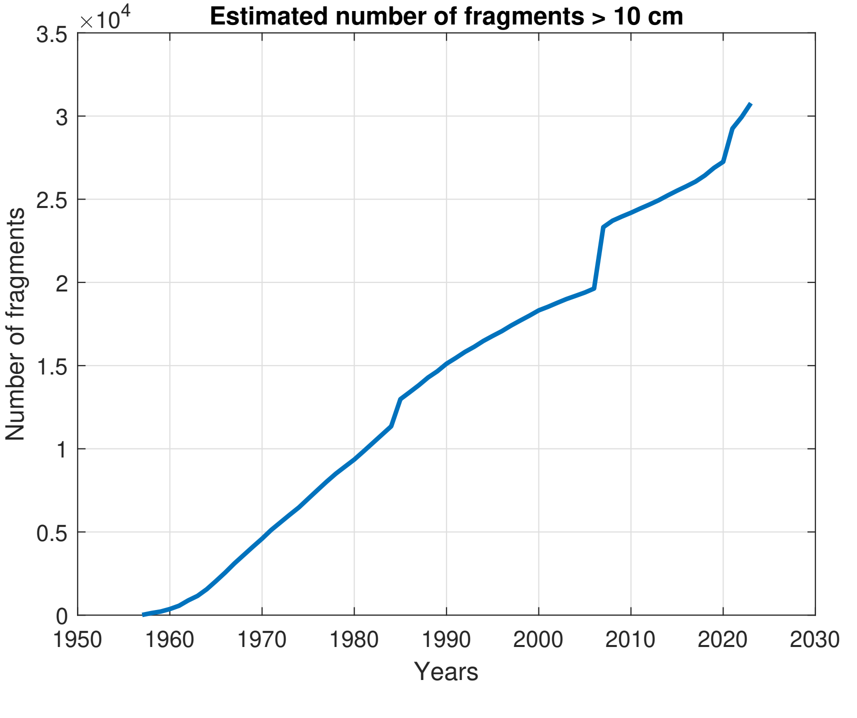

FIGURE A.8. Estimated number of fragments larger than 10 cm

A.6 *Self-destruction and anti-satellite tests*

A significant amount of orbital debris has been intentionally generated beyond the normal operational release of objects. This type of debris originates from the deliberate destruction of satellites. An example is a series of Soviet Union Cosmos satellites, which incorporated self-destruction explosive charges. Some Cosmos satellites, particularly military ones, were equipped with self-destruct mechanisms for security reasons. These mechanisms could be activated in cases of system failure, risk of capture by adversaries, or upon mission completion. The self-destruction typically involved an explosive charge designed to fragment the satellite into smaller pieces. According to the NASA breakups database (Anz-Meador et al., 2022), there have been 51 self-destruction events of Cosmos satellites, resulting in a total of 2,109 cataloged debris pieces.

The other intentional source of orbital debris has been the testing of direct-ascent anti-satellite (DA-ASAT) weapon systems. These systems involve modified or specialized missiles capable of reaching altitudes well above 100 km. Such missiles can either directly collide with a spacecraft (kinetic weapons) or damage it through the explosion of a warhead a broad area. Four nations: the US, Russia, China, and India, have conducted DA-ASAT tests(see Table A.3). The first true DA-ASAT tests was conducted by the US in 1959, when a missile launched from a B-47 bomber came within four miles of the Explorer VI satellite, demonstrating the feasibility of anti-satellite weapons.

TABLE A.3. Direct-ascent ASAT tests

Date	Country	Target	Altitude	Cataloged debris
13 September 1985	US	Solwind P-78	555	1,150
11 January 2007	China	Feng-Yun 1C	865	3,449
21 February 2008	US	USA-193	247	174
27 March 2019	India	Microsat-R	300	129
15 November 2021	Russia	Cosmos-1408	485	1,500

Source: Bongers and Torres (2023)

On 13 September 1985, the United States conducted a direct-ascent anti-satellite (DA-ASAT) test targeting the *Solwind P78-1*, a U.S. gamma-ray spectroscopy satellite. The satellite, weighing 850 kg and orbiting at an altitude of 555 km, was destroyed by an ASM-135 ASAT missile launched from an F-15A aircraft. The test resulted in 1,150 (initially 285) cataloged pieces of orbital debris. On 21 February 2008, the U.S. conducted another DA-ASAT test, known as Operation Burnt Frost, targeting the malfunctioning U.S. reconnaissance satellite *USA-193*, which had a mass of approximately 2,300 kg. The satellite was intercepted at an altitude of 247 km using a modified RIM-161 Standard Missile 3 launched from a naval vessel. This test produced 174 pieces of orbital debris that were cataloged by the U.S. military.

China was the second country to test DA-ASAT weapon systems (Weeden, 2020a) as the Soviet Union focused on the development of battle-stations (*Salyut-3*), Killer satellites (Cosmos-185, 242, 375, 2521, 2536). The most important test took place on 11 January 2007, when China destroyed its own *Feng-Yun 1C* weather satellite, which had a masst of 750kg and was at an altitude of 865 km. This test resulted in the creation of 3,438 cataloged pieces of debris (NASA, 2007). On 13 November 2015, Russia conducted its first DA-ASAT test, followed by additional tests in December 2018, April 2020 and December 2020 (Kommel and Weeden, 2020). The most recent DA-ASAT test by Russia occurred on 15 November 2021, resulting in the destruction of a defunct Soviet satellite (*Cosmos-1408*) at an altitude of 485 km, producing 1,500 pieces of tracked debris according to the USSC (NASA, 2022).

Finally, the last country to join this club was India. India joined in 2019, with an DA-ASAT test in March 2019 that destroyed Microsat-R at an altitude of 300 km (Pfrang and Weeden, 2020b). This test created a reported 129 tracked pieces of debris, but given the low altitude of the test, the decay rate is high (Jiang, 2020).

Debris fragments have also been produced by orbital weapon systems. For instance, on 20 October 1968 a Soviet Union killer satellite (*Cosmos 252*) attacked *Cosmos-248*, producing a total of 252 tracked debris fragments (Bongers and Torres, 2023).

A.7 *Debris larger than 10 cm*

Debris larger than 10 cm, $D_{1,t}$, represents the population of debris estimates by the model. This includes fragments larger than 10 cm, derelict satellites, and rocket bodies. The rationale is that for calibrating the parameters of the debris evolutionary model we use information about cataloged debris. Given the existing space surveillance technology, only debris larger than 10 cm can be tracked, although some smaller pieces can also be tracked in LEO. Therefore, we assume that cataloged debris are those larger than 10 cm, and hence this is the debris type estimates by the model.

Figure A.9 plots the estimated number of debris larger than 10 cm for the period 1957-2023, including cataloged debris from ASAT tests. The jumps observed in the time series correspond to debris fragments created by DA-ASAT tests, which are totally exogenous. It can be observed that the estimated number of debris by the model is significantly larger than those reported by Space-Track or NASA.

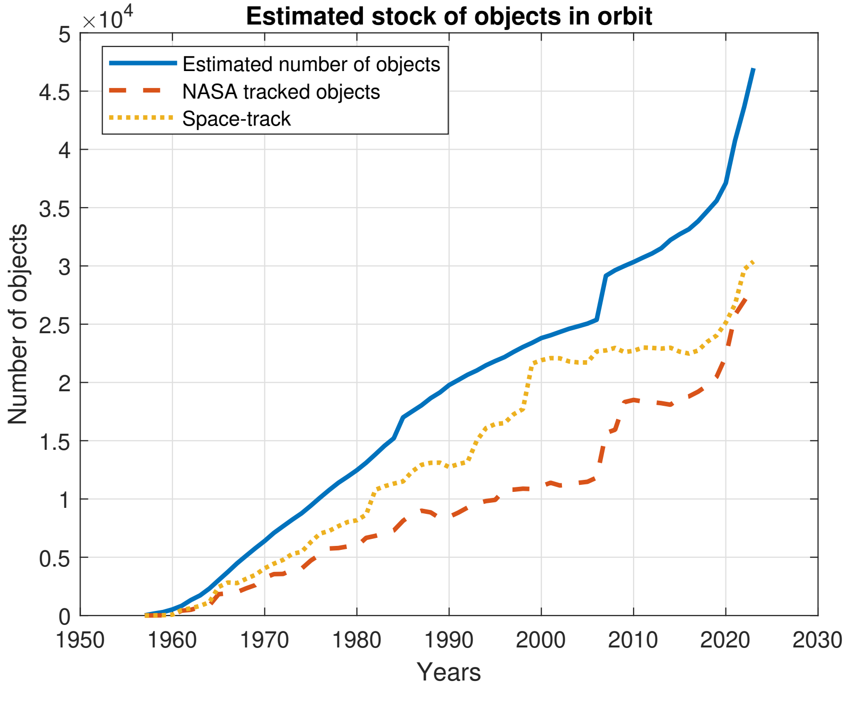

FIGURE A.9. Estimated number of objects in orbit estimated by the model, tracked by NASA, and tracked by the US Space Forces

A.8 *Debris larger than 1 cm*

From the estimated number of debris larger than 10 cm and using the scale factor indicated above, we obtain the estimated number of debris larger than 1 cm, which is the relevant size of debris to estimate the risk of collision. Figure A.10 plots the estimated historical trajectory debris larger than 1 cm, including fragments, rocket bodies, and derelict satellites, resulting from the calibrated model. The estimated figure for the year 2023 is 1,005,750, a number close to the 1 million orbital debris pieces larger than 1 cm estimated by the ESA by December 2023.

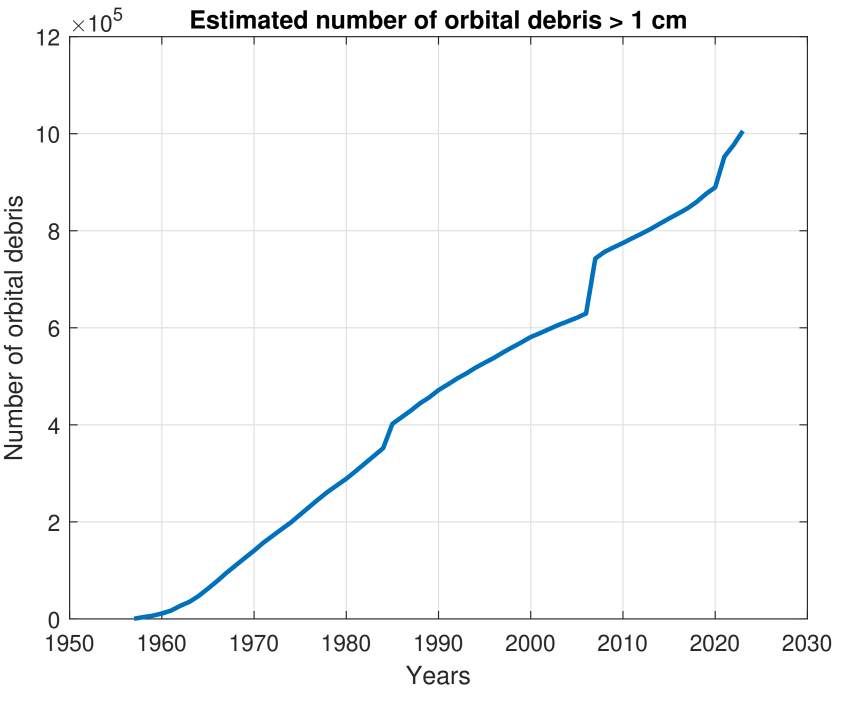

FIGURE A.10. Estimated number of orbital debris larger than 1 cm

APPENDIX B: INITIAL VALUES

The model is simulated taking 2023 as the base year. For the simulation of the trajectories of the model variables, we need initial values for the state variables and other relevant variables for the initial year. For population (i.e., labor), the figure for the year 2023 is taken from the United National Population Division (World Population Prospects, 2024), with a value of 8,056 million, and an asymptotic population value of 10,200 million. The initial value for World GDP is taken from the World Bank Economic Indicators, and is 184.65 trillions in 2023 international US$. Other sources of World GDP estimation are the IMF and Penn World Tables. From the IMF Investment and Capital Stock Dataset, 1960-2019, World GDP was 124.2 trillions in 2017 international US$ for the year 2019 (175.53 trillions international US$ at current 2023 prices). This figure as estimated in the Penn World Tables (PWT 10.01, Feenstra et al. 2015), for World GDP in the year 2019 is of 125.5 trillions 2017 international US$ (177.37 trillions in 2023 international US$). All three estimates are fairly similar, taking into account that the estimate from the World Bank is for the year 2023, whereas the estimates from the IMF and PWT are for the year 2019.

World capital stock is taken from the IMF Investment and Capital Stock Dataset, 1960-2019, as the sum of private and public capital for the year 2019, with a value of 316.25 trillion 2017 international US$ (446.95 trillion in 2023 international US$). The corresponding figure from the PWT is higher 535.12 trillions 2017 international US$, (756.27 trillion in 2023 international US$). Comparing both databases, we find a large difference in the estimates for the capital stock. Using data from the IMF, the World capital/GDP ratio is 2.55, whereas using the PWT, the ratio is 4.26.

We calculate Earth capital and space capital using the steady state proportion as follows. First, as indicated in appendix C, labor share is fixed to be 0.65. Given the assumption of constant returns to scale, the capital share, for Earth and space capital, is 0.35. Next, from the Euler equations for capital investment in steady state, with no risk of collision, we obtain that,

$$(1+g_c)^\sigma = \beta\left(\alpha_1 \frac{y}{k} + 1 - \delta_k\right) \tag{A.8}$$

and

$$(1+g_c)^\sigma(1+g_q) = \beta\left(\alpha_2 \frac{y(1-m)}{s} + 1 - \delta_s\right) \tag{A.9}$$

for the Earth capital and space capital, respectively. We assume that consumption growth rate is 2%. Using the calibrated values for the parameters (Appendix C), and taking into account that the launch cost is 30% of total investment in space capital, we obtain that,

$$(1.02)^{1.5} = 0.9852 \left(0.3479 \frac{184.65}{k} + 1 - 0.07 \right) \tag{A.10}$$

and

$$(1.02)^{1.5} \times 1.03 = 0.9852 \left(0.0021 \frac{184.65 \times 0.7}{s} + 1 - 0.15 \right) \tag{A.11}$$

From that we obtain that initial Earth capital stock is estimated to be $k = 552.747$, and that space (satellites) capital stock is $s = 1.203$, trillion international US dollar. The fraction of Earth capital is 99.78% of total capital, with space capital accounting for the rest 0.22%. The stock of space capital is small given the small ouput-satellite elasticity and the fraction of launch costs. Table B.1 summarizes the initial values for the base year (2023) used for the solution of the model.

TABLE B.1. Initial values for the year 2023

Variable	Value	Units	Source
World GDP	184.65	Trillions international US$	World Bank
Earth Capital stock	555.6987	Trillions international US$	Model
Space capital stock	1.1959	Trillions international US$	Model
Launch cost	0.30	Percentage of total cost	Adilov et al. (2022)
World Population	8,056	Millions inhabitants	United Nations
Operational satellites	8,500	Units	ESA
Number of launches	217	Units	NASA
Derelict satellites	3,500	Units	ESA
Rocket bodies	2,050	Units	NASA
Orbital debris > 10 cm	36,500	Units	NASA/ESA
Orbital debris > 1 cm	1,036,500	Units	NASA/ESA

Appendix C: Calibration of economic parameters

For the calibration of economic parameters, it is necessary to take into account that we are modeling the global economy, including both the Earth and space. Outer space is a global commons and any country or firm with enough financial resources and the necessary technology can access space. However, only a few countries have spacecraft launch capabilities, and not all countries operate satellites. However, services produced by satellites are consumed worldwide. The US is the absolute leading spacefaring country. Private spacefaring companies are also dominated by US companies, such as SpaceX. However, an increasing number of countries are also developing space industries and gaining spacecraft launch capabilities.

The economy module of DISE-2024 includes some standard parameters in the macroeconomic literature, although it also includes some new parameters related to the space sector. This set of parameters includes the social pure discount factor, the elasticity of marginal consumption, the technological parameters of the production function, and the physical capital and satellite depreciation rates. For that set of parameters, we use standard values from the literature. Additionally, the model includes two technological growth processes: Total Factor Productivity (TFP) and Investment-Specific Technological Change (ISTC) in satellites, and the labor growth rate (see Appendix E).

Table C.1. Baseline calibration of the economic parameters of DISE-2024

Parameter	Definition	Value	Source
ρ	Pure time preference parameter	0.015	Nordhaus (2008)
σ	Intertemporal marginal consumption rate	1.50	Nordhaus (2008)
α_1	Capital share	0.3479	BEA
α_2	Satellite share	0.0021	BEA
δ_k	Capital depreciation rate	0.07	Standard
δ_s	Satellite depreciation rate	0.15	NASA
μ	Conversion parameter	4,941	Internal

C.1 *The pure rate of time preference (ρ)*

The pure rate of time preference reflects how individuals value present consumption compared to future consumption. The rate of time preference indicates the degree to which people prefer to receive goods or utility sooner rather than later, that is, it is a measure of the impatience of households. This reflects individual preferences for present consumption over future consumption, indicating how much current utility is valued compared to future utility. A higher rate implies a stronger preference for the present compared to the future. The relationship between the pure rate of time preference and the social discount rate is a fundamental aspect of economic theory, particularly in the context of public policy and welfare economics. The social discount is the rate used to convert future costs and benefits into present values when evaluating public projects and policies. It represents society's preference for current benefits over future ones. Therefore, this is a key parameter for the design and implementation of mitigation policies for emissions which effects are long-lasting.

The social discount rate often incorporates the rate of time preference along with considerations for economic growth and risk. A higher rate of time preference implies a higher social discount rate, suggesting that society prioritizes present benefits over future ones. This can lead to less investment in long-term projects, such as infrastructure or environmental sustainability. Conversely, a lower rate of time preference (or higher growth expectations) may result in a lower social discount rate, allowing for greater consideration of long-term benefits. The choice of the social discount rate also has significant implications for intergenerational equity. A high discount rate may prioritize current generations at the expense of future ones, while a lower rate can promote policies that consider the welfare of future generations more equitably.

The appropriate level of the social discount rate is an important debate in macroeconomics and, especially, in environmental economics, at it is an indicator of how society values future benefits relative to present ones. Some authors argue for a lower rate to account for the welfare of future generations, while others emphasize the uncertainties associated with long-term forecasts. In the literature, we find two alternative approaches for determining the social discount rate: the prescriptive and the descriptive approaches. The prescriptive approach derives a normative social discount rate based on ethical considerations (Ramsey, 1928; Stern, 2006). The descriptive approach calculates the social discount rate based on observed interest rates. The social discount rate based on ethical considerations is obtained through surveys of academic experts and is much lower than that based on market interest rates. In contrast, the descriptive approach relies on observed interest rates, resulting in a much higher social discount.

The social discount rate has proven to be a key parameter for assessing the implications of climate-change policies. Estimated values range between the 2% per year used by Weitzman (2007) and the 0.1% used by Stern (2006). The US Interagency Group uses a central value of 3%, with a low bound of 2.5% and an upper bound of 5%. Barro (2015) argues that the use of low discount rates is inconsistent with empirical evidence and no supported by the theoretical side.

With a CRRA instantaneous utility function, we have that in steady state $r_t = \rho + \sigma g_{c,t}$, where r_t is the discount rate (interest rate) representing the net present value of a dollar in t year, σ is the intertemporal marginal consumption rate, and $g_{c,t}$ is the growth rate. This is the so-called Ramsey equation. With a steady-state growth of 2% and a relative risk aversion parameter of 2, the discount rate ranges between 6% and 4.1%, aligning with values commonly used in standard Dynamic Stochastic General Equilibrium (DSGE) macroeconomic models. For the baseline calibration, we fix the value of ρ to be 1.5% per year.

The Ramsey equation is obtained as follows. The problem solved by an infinitely-lived representative household can be formulated as,

$$\max_{c_t} \sum_{t=0}^{\infty} \left(\frac{1}{1+\rho} \right)^t U(c_t) \tag{C.1}$$

subject to the following budget constraint,

$$c_t + b_t = y_t + (1 + r_{t-1}) b_{t-1} \tag{C.2}$$

where b_t is the stock of savings, y_t is labor income, and r_t is the interest rate of savings. It is assume a utility function of the Constant Relative Risk Aversion (CRRA) type, defined as:

$$U(c) = \frac{c^{1-\sigma}}{1-\sigma} \quad (\sigma \neq 1) \tag{C.3}$$

where σ is the coefficient of relative risk aversion. The first-order condition for maximizing utility requires that the marginal utility of consumption is equated across time. The marginal utility of consumption at time t is given by:

$$U'(c_t) = c_t^{-\sigma} \tag{C.4}$$

First order conditions are derived by solving the following Lagrange problem

$$\mathcal{L} = \left(\frac{1}{1+\rho} \right)^t \frac{c^{1-\sigma}}{1-\sigma} - \lambda_t (c_t + b_t - y_t - (1 + r_{t-1}) b_{t-1}) \tag{C.5}$$

First order conditions are:

$$c_t^{-\sigma} - \lambda_t = 0 \tag{C.6}$$

$$-\left(\frac{1}{1+\rho}\right)^t \lambda_t + \left(\frac{1}{1+\rho}\right)^{t+1} (1+r_t)\lambda_{t+1} = 0 \tag{C.7}$$

Combining both first-order conditions, we get,

$$c_t^{-\sigma} = \frac{1+r_t}{1+\rho} c_{t+1}^{-\sigma} \tag{C.8}$$

taking logarithms of both sides yields:

$$-\sigma \ln(c_t) = \ln(1+r_t) - \ln(1+\rho) - \sigma \ln(c_{t+1}) \tag{C.9}$$

Let $g_{c,t} = \frac{c_{t+1}}{c_t} - 1$ denote the growth rate of consumption. For small $g_{c,t}$, we have that:

$$\ln(c_{t+1}) = \ln(c_t) + \ln(1+g_{c,t}) \approx \ln(c_t) + g_{c,t} \tag{C.10}$$

Substituting into the logarithmic expression:

$$-\sigma \ln(c_t) = \ln(1+r_t) - \ln(1+\rho) - \sigma(\ln(c_t) + g_t) \tag{C.11}$$

Finally, assuming that r_t and ρ are small, $\ln(1+r_t) \approx r_t$, and $\ln(1+\rho) \approx \rho$, we arrive to

$$r_t = \rho + \sigma g_{c,t} \tag{C.12}$$

C.2 *Intertemporal marginal consumption substitution parameter (σ)*

This parameter reflects the curvature of the utility function, which is the inverse of the elasticity of marginal utility of consumption. See, for instance, Szpiro (1986), Dasgupta (2008), and Weitzman (2007, 2009). A higher σ (a lower elasticity of intertemporal substitution) means the household is less willing to substitute consumption intertemporally. The use of a CRRA instantaneous utility function makes the value of the intertemporal substitution is equal to the inverse of the coefficient of relative risk aversion, both reflecting the curvature of the utility function. Formally, the elasticity of marginal utility of consumption is defined as the curvature of the utility function,

$$\sigma = -c\frac{U''(c)}{U'(c)} \tag{C.13}$$

where $U'(c_t) = c_t^{-\sigma}$ and $U''(c_t) = -\sigma c_t^{-\sigma-1}$. Typically, σ is assumed to be independent of the reference consumption path, c_t, although there is no clear reason why it should be so (Dasgupta, 2008). In standard models, for the class of utility functions in which σ is constant, the larger this parameter, the greater the curvature of the utility function. For the typical specification of the utility, U(C) is bounded above but unbounded below if $\sigma > 1$, while the reverse holds if $\sigma < 1$.

In the literature, the relative risk aversion parameter σ takes values between 1 (a logarithmic instantaneous utility function) and 3. For example, Stern (2006) use a value of 1, Nordhaus (2008) uses a value of 1.5, whereas Nordhaus (2017) uses a value of 2. In our baseline calibration, we set the value of σ to 1.5 in the baseline calibration. Most studies that have quantified global climate change impacts assume $\sigma = 1$; however, there is a growing number of studies that rely on the elasticity of marginal utility of consumption above the unity (e.g., Cline (1992) assumed $\sigma = 1.5$). Evans (2005) estimates the elasticity of marginal utility of consumption for 20 OECD countries based on the structure of personal income tax rates, finding an average value of around 1.4, with a range from a value of 1.00 for Ireland to 1.82 for Australia. However, other authors use large values. For instance, Mehra and Prescott (1985) estimate values greater than 10.

The literature has developed a variety of alternative methods to estimate these parameters: Direct estimation of the consumption Euler equation (Hansen and Singleton, 1982), methods based on income tax data (Stern, 1977), approaches using asset returns data (Mehra and Prescott, 1985), direct survey-based methods (Barsky et al., 1997), or based on the labor supply distortions by tax (Chetty, 2006). Stern (1977) used income tax data for the UK and suggested a value of σ around 2, with a range between 1 and 10. Barsky et al.

(1997) surveyed 11,707 middle-aged respondents in the US to elicit measures of risk tolerance, the elasticity of intertemporal substitution, and time preference. They found that there is substantial heterogeneity in these preference parameters. In their study, they report the mean of the coefficient of relative risk aversion ranging form 0.7 to 15.8, with the average at about 4.0.

Finally, some authors relax the assumption of a time-separable utility function and instead use an Epstein-Zin utility function with dynamic preferences (Epstein and Zin, 1989). This utility function allows for the separation of the risk aversion and the intertemporal elasticity of substitution and hence makes it possible to investigate how alternative values for these two parameters affect households' the intertemporal decisions. See, for example, Ackerman et al. (2013).

C.3 *Output-capital elasticity parameters (α_1, α_2)*

For the calibration of technological parameters, we proceed as follows. First, we assume that capital and labor income shares are fixed over time. Dynamic macroeconomic models typically assume that output-input elasticities remain constant over time. With a Cobb-Douglas technology, technological parameters representing the elasticity of output with respect to capital and labor are equal to the capital and labor income share, respectively.

We fix the labor share to be 0.65. Given the assumption of constant returns to scale, this means that the sum of the technological parameters for Earth capital and space capital is 0.35 (i.e., $\alpha_1 + \alpha_2 = 0.35$). Corrado et al. (2023) calibrate the space sector's share of the overall economy at 0.0056. The Bureau of Economic Analysis (BEA, 2023) estimates that space industry contributed 129,9 billion dollars to the US economy in 2021 (0.6% of GDP), supporting a total of 360,00 full- and part-time jobs in the private space industry. Space Foundation (2023) estimates that the global space economy had a total impact of $546 billion for the year 2022. The satellite Industry Association (SIA, 2023) estimates that the global space economy accounted for $384 billion for the year 2022. Using this information, we allocate the capital share between Earth capital and space capital. The elasticity of output with respect to satellites equipment is calculated as $\alpha_2 = 0.35 \times 0.006 = 0.0021$. Hence, the elasticity of output with respect to Earth capital is $\alpha_1 = 0.35 - 0.0021 = 0.3479$. Nozawa et al. (2023) calibrated a Cobb-Douglas production function including labor, capital and satellites, and used a value of 0.002 for the elasticity of output to the stock of satellites.

C.4 *Capital depreciation rates (δ_k, δ_s)*

Typically, dynamic macroeconomic models assume that capital stock depreciates at a constant rate over time, although some models consider a non-constant depreciation rate due to a time-varying use of capital over the business cycle or to structural changes driven by technological progress, which alter the proportion of the different types of capital assets used in the economy. Capital depreciation rates greatly vary depending on the type of capital asset (Fraumeni, 1997). Structures typically show a relatively low depreciation rate compared to equipment, while capital assets related to information and communication technologies (ICTs) usually have a much higher depreciation rates. For instance, the European Central Bank (2006) estimates an average capital depreciation rate of 4.6% per year in the Euro Area, corresponding to an average lifetime of capital stock around 20 years. By asset type, depreciation rates are approximately 2% for housing, 3% for non-residential structures, 14% for equipment, and 24% for other assets including software.

Capital depreciation rates also vary across countries, as they have different combinations of capital assets. However, depreciation rates by asset type are fairly similar, and only in extreme climate conditions can depreciation rates vary substantially. In general, it is assumed that depreciation rates increase with income levels. Gupta et al. (2014) estimate that depreciation rate of private capital ranges from 4.25% in low-income countries, 8.10% in middle-income counties, to 10.41% in high income countries. For public capital, depreciation rates range from 2.5% in low-income, 3.5% in middle-income, to 4.59% in high-income countries. In the estimation of capital stocks in the Penn World Tables (PWT), depreciation rates differ across assets, across countries and over time (Feenstra et al., 2015), with average estimated values of 2% for structures, 12.6% for machinery and 31.5% for computers and software.

In the literature, standard macroeconomic models use values in the range of 7-10% per year for aggregate capital depreciation rate (or approximately 0.025 per quarter) in the case of developed economies. For the world economy, which not only include developed economies but also developing economies, the depreciation rate would be at the lower range. Therefore, the depreciation rate of capital other than satellites (what we call Earth's capital), δ_k, is set at 0.07.

In calibrating the depreciation rate of satellites, we also take into account that they are not homogeneous and exhibit specific characteristics that influence their average operational life. The extreme conditions in outer space and technical characteristics of satellites determine their life-span, in additions to differences in design depending the mission. A satellite's life-span depends on its type, as well as electrical, mechanical, physical and gravitational factors (Gallois, 1987). One important limitation to a satellite's operational life is fuel capacity. Indeed, some derelict satellites may remain functionally impact and capable of delivering services, but are rendered inoperable due to fuel depletion, which prevents repositioning to the targe orbit. Lifespans vary significantly, from as little as 6 months for CubSats (miniaturized satellites), to up to 15 years of GEO satellites. For LEO satellites, the lifespan typically ranges from 3 to 8 years. For example, the expected lifespan of starlink satellites is of 5-7 years. Bongers and Torres (2023) assume an average lifetime of 8 years for all satellites, leading to an annual depreciation rate of 0.1733. Nozawa et al. (2023) use a depreciation rate for satellites of 0.216, based on an assumed average lifespan of 4.64 years for LEO satellites. In this study, we assume a depreciation rate of 15% per year ($\delta_s = 0.15$).

C.5 *Conversion parameter (μ)*

The model includes both economic and physical measurement of the same variable. While economic variables are measured in monetary values (trillions of international dollar), physical variables are measured in units. One characteristic of the theoretical model is that for obtain a numerical solution it is necessary to work simultaneously with both output-value and physical variables. This forces the introduction of a mapping function between both types of variables. As a reference, we use the value of satellites and the number of satellites. This mapping is extended to satellites destroyed by collisions, new satellites inserted in orbit, and launches.

The conversion parameter from economics variables to physical variables is calculated internally, dividing the initial number of satellites in units, S_0, by the initial value of the stock of satellites measured in trillions international US$, s_o. Hence, $\mu = 8,500/1.72 = 4,941.9$. This value is fixed throughout the simulation horizon. The inverse of this number can be interpreted as a proxy of the unit value of satellites, including the associated capital assets used in the space sector.

Appendix D: Calibration of physical parameters

For the calibration of physical parameters, we primarily rely on data from NASA Breakups Database (Anz-Meador et al., 2022) and ESA's DISCOS database (DISCOSweb), supplemented by additional sources such as the Union of Concerned Scientists (UCS) Satellite Database and Jonathan C. McDowell's satellite datasets. To calibrate the number of fragments generated by breakup or collision events, we use information on cataloged debris. We assume that debris larger than 10 cm is adequately represented by cataloged fragments. Accordingly, the calibrated number of fragments corresponds to debris exceeding 10 cm in size. Using the proportional parameter Γ, we estimate the population of debris larger than 1 cm based on the population of debris larger than 10 cm. The calibrated physical parameters are presented in Table D.1.

Table D.1. Baseline calibration of the physical parameters of DISE-2024

Parameter	**Definition**	**Value**	**Source**
η	Satellites per launch	13.6	NASA
δ_w	Derelict satellites natural depreciation rate	0.00015	Lafleur (2011)
δ_z	Rocket bodies nautral decay rate	0.00015	Lafleur (2011)
δ_f	Fragments debris natura decay rate	0.01	Lafleur (2011)
θ	Collision risk parameter	1.25×10^{-10}	ESA
χ	Fraction of abandoned satellites	0.40	ESA
φ	Body rockets per launch	0.60	ESA
ε_w	Fraction of dead satellites breakups	0.0010	ESA
ε_z	Fraction of body rocket breakups	0.0012	ESA
ω	Number of fragments per launch	4.00	ESA
ϕ_w	Number of fragments per derelict satellite breakup	40.6	ESA/NASA
ϕ_z	Number of fragments per rocket body breakup	100.2	ESA/NASA
γ_s	Number of fragments per operational satellite collision	70	ESA/NASA
γ_w	Number of fragments per derelict satellite collision	70	ESA/NASA
γ_z	Number of fragments per rocket body collision	70	ESA/NASA
v_t	Collision avoidance proportion	0	Baseline
Γ	1cm to 10 cm debris proportional parameter	32.3	ESA

D.1 *Satellites per launch (η)*

Current technology for inserting satellites into orbit is entirely based on rocket launch systems. Rockets launch vehicles consist in several stages (from two to four). The first stage(s) provide the initial thrust and separate after fuel is exhausted. The upper stage(s) continue to propel the satellite toward its target orbit. Typically, a single rocket carries more than one payload, depending on the rocket's capacity and the payloads' size. The number of payloads per rocket launch has significantly increased in recent years due to advancements in rocket design, more powerful launch systems, and standardization and miniaturization of satellites. Recent launch systems like SpaceX's Falcon 9 and Falcon Heavy can carry dozens or even hundreds of payloads in a single launch, driven by the rise of small satellites and cubesats as well as the enhanced power of rocket engines. This trend reflects the growing demand for cost-effective access to space and innovations in payload integration systems.

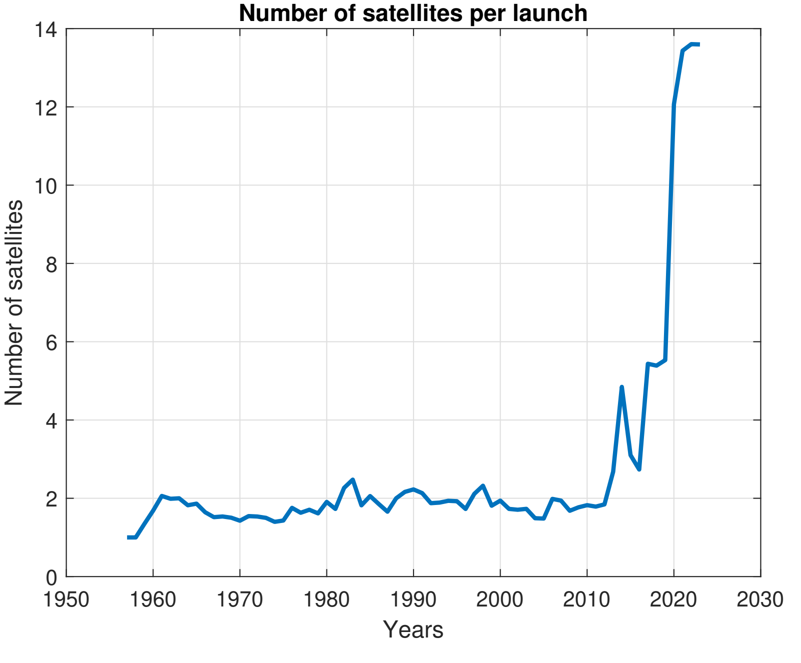

FIGURE D.1. Number of satellites per rocket launched

Figure D.1 plots the number of payload per launch for the period from 1957 to 2023. It can be observed that for most of the period, the number of satellites per launch remained almost constant around an average of 2 payloads per launch. However, this stable trend began to change dramatically starting in 2015, increasing to more than 10 satellites per rocket in recent years, a sharp change mainly associated with the launch of the satellites of the Starlink constellation.

For the calibration of the model, instead of using the average number over the historical sample period, we use the ratio corresponding to the last year of the period, implicitly assuming that the observed change occurring in recent years will be permanent. The number of satellites inserted into orbit during the year 2023 is $H_0 = 2,950$, and the number of launches is $L_0 = 217$. Therefore, $\eta = H_0/L_0 = 13.6$. This value is kept fixed throughout the simulation horizon, as we have no information on how this ratio will change in the future.

D.2 *Fragments natural decay rate* (δ_f)

The accumulation process of orbital debris critically depends on their survival time in orbit, which is a function of their natural decay rate. The computation of the decay rate of objects in orbit is a controversial issue in space engineering. The value of this parameter varies dramatically depending on the altitude of the object, making it difficult to obtain an average decay rate for the totality of objects in Earth's orbit. The decay rate of an object in orbit depends on a large number of factors, most of which are difficult to estimate accurately or are highly variable over time, even on an hourly basis. As pointed out by Niccolai and Mengali (2024), the estimation of the decay rate of an object in orbit is a very challenging task due to the difficulty to accurately modeling atmospheric properties and complex orbital dynamics. On the other hand, as pointed out by Lafleur (2011), the lifetime differs significantly between intact satellites and fragments because fragments typically have larger surface-area-to-volume ratios. Therefore, we distinguish the natural decay rate of small fragments from that of large intact objects, such as rocket bodies and derelict satellites.

The natural decay rate of orbital objects depends on several factors, including the altitude (or atmospheric density), orbit circularity, mass, area, solar radio flux, and geomagnetic index. The most important factor is the altitude due to the atmospheric drag, which results from the interaction of the object with the few air molecules present at high altitudes. This drag is very high at low altitudes but extremely low at high altitudes. Atmospheric drag tends to reduce the altitude of an object in orbit (and also circularize the orbit). The drag reduces the velocity of the object and pulls it towards the Earth. For relative low altitudes (below 1,000 km), gravitational effects of the Earth is the main factor affecting the behavior of objects. However, for high orbit, such as GEO, the gravitational effects of the sun and the moon, as well as solar radiation, are the dominant forces affecting dynamics of object at that altitude.

The force of gravity acting on an object in orbit serves as a centripetal force. Hence, in the case of a circular orbit, by applying Newton's second law along with the relationship between centripetal acceleration and the object's linear velocity, the orbital velocity of the object can be expressed as,

$$v = \sqrt{\frac{GM}{r}} \tag{D.1}$$

where G is the gravitational constant ($6.674 \times 10^{-11}\ \ N \times m^2 \times kg^{-2}$), M is the mass of the Earth ($5.98 \times 10^{24}\ \ kg$), and r is the radius of the trajectory (the distance of the object to the center of the Earth), with the Earth's radius equal to 6,378 km. As a result of previous expression, the conserved mechanical energy of the system (without considering any form of mechanical energy dissipation), is given by,

$$E = -\frac{GMm}{r} + \frac{1}{2}mv^2 = -\frac{GMm}{2r} \tag{D.2}$$

where m is the mass of the object measured in kg. Atmospheric models based on previous calculations are used to predict the decay rate of objects. The decay rate of an object in orbit is a function of atmospheric density at each point along the orbit, the effective cross-sectional area perpendicular to the direction of motion, A, the mass m, and the drag coefficient C_D, which usually estimated from a free molecular flow model. C_D is generally assumed to be equal to 2.2 (Cook, 1965; Jacchia, 1972), although this can vary depending on altitude. The combination of these three parameters results in the so-called ballistic coefficient (King-Hele, 1987). The drag force F_D, is calculated as,

$$F_D = \frac{1}{2}C_D A \rho v^2 \tag{D.3}$$

where ρ is the atmospheric density (a function of altitude, latitude, longitude, the season and time of the day, temperature, thermosphere composition, and the solar and geomagnetic activity), measured in kg/m^3, and v is the velocity measured in m/s. On average, for a given altitude, atmospheric density can be approximated as a function of two parameters: the solar 10 cm radio flux (F_{10}), and the geomagnetic index A_p. Most drag models use solar radio flux at 10.7 cm wavelength as a proxy for solar ultraviolet flux. The solar 10 cm radio flux varies between 70 (solar minimum conditions) and 250 (solar maximum conditions). The rate of energy loss due to drag can be calculate as,

$$\frac{dE}{dt} = -F_D v \tag{D.4}$$

Substituting for F_d, we have,

$$\frac{dE}{dt} = -\frac{1}{2}C_D \rho A v^3 \tag{D.5}$$

For the case of near-circular orbits, the semi-major axis a is approximately equal to the radius of the central body plus the altitude ($a \approx r + h$). The semi-major axis is defined as the distance from the center of an ellipse to the farthest point along its major axis. As energy is lost due to atmospheric drag, the semi-major axis gradually decreases, leading the object to spiral closer to Earth,

$$\frac{da}{dt} = \frac{1}{GMm}\frac{dE}{dt} = -\frac{1}{2GMm}C_D \rho A v^3 \tag{D.6}$$

For a near-circular orbit we have that $dh/dt \approx da/dt$, and therefore, the rate of altitude loss can be calculated as,

$$\frac{dh}{dt} = -\frac{1}{2GMm} C_D \rho A v^3 \tag{D.7}$$

The object acceleration or the decay orbit, is then calculated as,

$$Drag = \frac{1}{2}\frac{C_D \rho A}{m} v^2 \tag{D.8}$$

Doornbos et al. (2013) indicate that for the case of orbital debris, where both the mass and the area are unknown, it is more appropriate to estimate the inverse of the ballistic coefficient rather than the drag coefficient. The inverse of the ballistic coefficient, B, is defined as,

$$B = \frac{C_D A}{m} \tag{D.9}$$

Calibrating of the debris natural decay rate is a key issue in this analysis, as this parameter determines the natural reduction in the stock of debris and, hence, also affects the distribution of debris as a function of altitude is not homogeneous. The spatial density of debris shows that it is concentrated in the range 700-900 km (NASA, 2020). Bongers and Torres (2023) use the average of this figure as a reference, and therefore estimate the average lifetime of debris at around 150 years. Assuming straight-line decay, this implies an annual decay rate of 0.0067. This is consistent with the value for the general atmospheric decay parameter of 0.0062 used by Lewis et al. (2009) in the Fast Debris Evolution (FADE) model.

The Australian Space Weather Agency (1999) estimated that the lifetimes of space objects vary significantly with altitude: approximately 1 day at 200 km, 1 month at 300 km, 1 year at 400 km, 10 years at 500 km, 100 years at 700 km, and 1000 years at 900 km. Rao and Rondina (2023) use data from ESA regarding the residence time of objects in orbit and calculate a share-weighted decay rate of 7.4% per year for the 600-650 km shell, 5% for the 650-700 km shell, and 3% for the 700-750 shell. Lafleur (2011) calculates an average debris decay rate for objects in LEO (up to 2,000 km) using the ballistic coefficient, assuming a representative value of 1.8 kg/m^2 for fragments. Based on this, he derives drag coefficient under both solar-maximum and the solar-minimum conditions, weighted by the distribution of objects at different orbit altitudes. Under the solar-maximum conditions, the average lifetime of debris fragment is of 46.9 years (a decay rate of 0.021), whereas under solar-minimum conditions, the average lifetime extends to 332.8 years (a decay rate of 0.003), resulting in a mean decay rate of 0.012 for LEO debris.

As an example, using the NASA's breakups database (Anz-Meador et al., 2022), we calculate the debris decay rate following the collision between *Iridium-33* and *Kosmos-2251* collision on February 10, 2009, was 1,347. This collision occurred at an altitude of 780 km. By January 1, 2011, 1,273 pieces of debris remained in orbit, representing 94% of the original debris, implying a decay rate of approximately 6% over two years, or about around 0.03 per year, assuming linear decay. Similarly, *Iridium-33* produced 528 cataloged fragments, with 492 pieces remaining in orbit by January 1, 2011 (or 93%), which corresponds to a decay of 7% in two years, or an annual decay rate of approximately 0.035. In contrast, the intentional destruction of *Fengyun-1C* during a military test on January 11, 2007, generated 3,037 pieces of cataloged debris. As of January 1, 2011, 2,932 pieces were still in orbit, 97% of the initial total. This implies a decay rate of just 3% over four years, or approximately 0.0075 per year. These differences in decay rates are mainly due to the altitude at which the debris was generated. While *Iridium-Kosmos* collision occurred at approximately 776 km, the *Fengyun-1C* even took place at a higher altitude of 860 km, where atmospheric drag is significantly lower, leading to slower orbital decay.

Table D.2 presents examples of the decay rate derived from NASA's breakups database, focusing on five fragmentation events. The first two cases correspond to debris generated by collision, while the remaining three involve breakups, two from rocket bodies (R/B) and one from a satellite. Even when the collision occurs at the same altitude, different decay rates are observed. For example, fragments from *Iridium-33* show a decay rate of 0.0557, whereas those from *Cosmos-2251* decay at a slower rate of 0.0389. These discrepancies highlight the role of orbital characteristic, particularly circularity, that is, de difference between the apogee and perigee, in influencing decay rate. In the case of the *Arabsat-4* rocket body breakup, a relatively low decay rate of 0.0065 is estimated, despite a perigee of just 495 km. For comparison, fragments from the *Telecom-3* rocket body breakup exhibit a much higher decay rate of 0.1863, even though the orbit ranges from a perigee of 265 km to an for an apogee of 5,010 km. This sharp contrast is likely driven by the low perigee, which exposes the debris to significant atmospheric drag. Finally, the breakup of a satellite in higher, more stable orbit, ranging between 960-1,015 km, results in a decay rate of 0.033, consistent with expectations for such altitudes.

Locke et al. (2024) assume that all fragments are spherical and model atmospheric drag using a simplified atmospheric density profile based on the ballistic coefficient, without accounting for solar radiation pressure. For small debris, they assume that a constant drag coefficient is 2.2. Prieto et al. (2014) provide a comprehensive review of existing methods for estimating drag coefficient.

TABLE D.2. Decay rates for selected case of the NASA's breakups database

Satellite	Apogee (Km)	Perigee (Km)	δ_f
Iridium 33	780	775	0.0557
Cosmos 2251	800	775	0.0389
Arabsat 4 Briz-M R/B	14,705	495	0.0065
Telecom 3 express MD2 Briz-M R/B	5,010	265	0.1863
Cosmos 1275	1,015	960	0.0033

An online calculator for satellite orbital decay, develop by the Australian Space Weather Agency, is avaliable at https://www.lizard-tail.com/isana/lab/orbital_decay/. Below, we present a MATLAB code adapted from the original QBASIC implementation provide by Australian Space Weather Agency for estimating decay rates of satellites in circular orbits below 500 km.

```
%*****************************************************************************
% ORBITAL DECAY
% Adapted from the QuickBasic code of the Australian Space Weather Agency
% Optimal path for orbital debris
%*****************************************************************************
% Get required input parameters
M = input('Mass (kg): ');
A = input('Area (m^2): ');
H = input('Altitude (km): ');
F10 = input('Solar Radio Flux (SFU) (40-400): ');
Ap = input('Geomagnetic A index (0-280): ');
% Print information
fprintf('ORBITAL DECAY - Model date/time: \%s\n', datestr(now));
fprintf('Mass = %.1f kg\n', M);
fprintf('Area = %.1f m^2\n', A);
fprintf('Initial height = %.1f km\n', H);
fprintf('F10.7 = %.1f, Ap = %.1f\n', F10, Ap);
% Column headings
fprintf('TIME        HEIGHT        PERIOD        MEAN MOTION        DECAY\n');
```

```
fprintf('(days)     (km)          (mins)     (rev/day)      (rev/day^2)\n');
% Constants
Re=6378000;              % Earth radius in km
Me=5.98e24;              % Earth mass in kg
G=6.67e-11;              % Gravitational constant
pi=3.1416;
T=0;                     % Initial time in days
dT=0.1;                  % Time increment in days
D9=dT*3600*24;           % Time increment in seconds
H1=10;                   % Height decrement for printing
H2=H;                    % Initial height for tracking
R=Re+H*1000;             % Orbital radius in meters
P=2*pi*sqrt(R^3/(G*Me)); % Orbital period in seconds
% Iteration for orbital decay
while H > 180  % Loop until satellite re-entry
    % Atmospheric scale height and density
    SH=(900+2.5*(F10-70)+1.5*Ap)/(27-0.012*(H -200));
    DN=6e-10*exp(-(H-175)/SH);  % Atmospheric density
    % Change in orbital period
    dP=3*pi*A/M*R*DN*D9;
    % Print results when height decreases by H1
    if H <= H2
        Pm=P/60;                 % Period in minutes
        MM=1440/Pm;              % Mean motion in rev/day
        nMM=1440/((P-dP)/60);    % New mean motion
        Decay=dP/dT/P*MM;        % Decay in rev/day$\hat{}$2
        fprintf('%6.1f  %8.1f  %8.1f  %10.4f  %10.5f\n',...
        T, H, Pm, MM, Decay);
        H2=H2-H1;                % Update print height
    end
    % Update values for next iteration
    P = P-dP;          % Update period
    T = T+dT;          % Update time
    R = (G*Me*P^2/(4*pi^2))^(1/3);  % Update orbital radius
    H = (R-Re)/1000;  % Update height in km
```

```
end
\% Print estimated lifetime of the satellite
fprintf('Re-entry after \%.1f days (%.2f years)\n', T, T/365);
```

D.3 *Derelict satellites natural decay rate (δ_w)*

The natural decay rate of intact objects in orbit differs significantly from that of orbital fragments. Fragments typically have a much larger surface-area-to-volume ratio compared to intact objects such as derelict satellites or rocket bodies. This characteristic leads to a smaller ballistic coefficient for fragments, which in turn results in much shorter orbital lifetime at a given altitude compared to intact objects. Conversely, intact objects have higher ballistic coefficients and thus remain in orbit for longer periods under similar conditions. Moreover, the drag coefficient also varies between fragments and intact objects. For, example, Locke et al. (2024) report that the space drag coefficient for intact spacecraft ranges form $C_D = 10$ for a 6U cubesat to $C_D = 35$ for a larger NOAA-20 type satellite. These values reflect the variation in size, shape, and surface properties that affect how objects interact with the residual atmosphere in low Earth orbit.

Lafleur (2011) estimates an average debris decay rate for intact objects in LEO (up to 2,000 km) using the ballistic coefficient value of 110 kg/m^2 as an approximate representation for satellites. From this, he derives the drag coefficient under both solar-maximum and the solar-minimum conditions. The values are weighted according to the distribution of satellites across different orbit altitudes. Under solar-maximum conditions, the average lifetime of derelict satellites is approximately 3,990 years (a decay rate of 0.00025), whereas under solar-minimum conditions, the average lifetime extends to about 24,850 years (a decay rate of 0.00004), resulting in a mean value for the natural decay rate of satellites in LEO of 0.000145. In calibrating δ_w we take Lafleur's (2011) estimated mean value for the natural decay rate as a reference. However, since the model incorporates all orbital regimes, the actual average natural decay rate is likely to be even lower. In the baseline calibration, this parameter has been fixed to 0.00015.

D.4 *Rocket bodies natural decay rate (δ_z)*

Natural decay rate of rocket bodies is calculated in a similar way to that for derelict satellites. Rocket bodies are intact objects and, therefore, their natural decay rate is lower than that of fragments. For rocket bodies, Locke et al. (2024) assume a drag coefficient of $C_D = 60$. This implies that the natural decay rate of rocket bodies is even lower than that of derelict satellites. However, Lafleur (2011) does not distinguish between derelict satellites and rocket bodies and instead uses an average mass-to-surface ratio for all intact objects. As no additional information is available, we adopt the average value estimated by Lafleur (2011), and hence, $\delta_z = 0.00015$.

D.5 *Risk of collision (θ)*

In the history of activity in outer space, a number of collisions have been reported. Collisions can occur between pieces of debris themselves or between debris and operational satellites. A risk of collision between operating satellites also exists, but in some cases they can be avoided by maneuvering, although many satellites have limited or no maneuvering capabilities. Several collisions with human-made debris have been reported in recent years, but some incidents likely remain undocumented. On February 10, 2009, an active US communications satellite (Iridium 33) collided with a non-operating Russian military communications satellite (Kosmos 2251). On January 22, 2013, a Russian small satellite (BLITS) was destroyed by a piece of debris from Fengyun-1C. On May 22, 2013, two CubeSats collided with debris (Ecuador's NEE-01 Pegaso and Argentina's CubeBug-1). A large number of potential collisions are avoided through frequent satellite and spacecraft maneuvering. Krisko (2007) estimated an average number of catastrophic collisions (involving a target and impactor larger than 10 cm) of 0.9, whereas the estimation from the DAMAGE model (Lewis et al., 2009) is 1.5, both covering the period 1957-2006. As a result of these collisions, numerous pieces of debris have been generated. Farinella and Cordelli (1991) estimated a value of $\theta = 3 \times 10^{-10}$, based on an estimated quantity of debris of 50,000.[1] This implies a number of satellite destruction per year of 0.2, given a collision probability ($\theta \times 50,000$) of 1.5×10^{-5}. Kawamoto et al. (2019) estimated that the current probability of collision is substantially higher. The total probability of collision of objects larger than 10 cm is approximately 0.1 for 800-900 km orbits, 0.05 for 900-1,000 km orbits, and 0.025 for 600-700 km orbits. Following Farinella and Cordelli (1991) we adopt a total probability of 0.2 (i.e., one fatal collision every 5 years) as the reference, which aligns with observed number of incidents (four collisions occurred in the period 1991 to 2009), resulting in a collision probability $\theta \times D = 6.6 \times 10^{-5}$. Pardini and Anselmo (2014) estimate that the risk of collision in LEO increased by a factor of 4.5 between 1980 and 2010.

Lafleur (2011) estimates a value of $\theta = 6.895 \times 10^{-10}$. Percy (2015) estimates a value of $\theta = 6.37 \times 10^{-10}$. Guyot and Rouillon (2024) use a value of $\theta = 4 \times 10^{-10}$. Bongers and Torres (2023) estimate a value of $\theta = 6.37 \times 10^{-11}$. In this paper, following Bongers et al. (2025), we adopt a value of $\theta = 1.25 \times 10^{-10}$, based on the observed number of registered collisions.

[1] Farinella and Cordelli (1991) estimate the number of collisions per unit cross section per year as the average collision velocity (10 km/s) divided by the volume of the circumterrestrial shell (1,800 km$\times 6 \times 10^8$ km^2).

D.6 *Fraction of abandoned satellites (χ)*

Defunct satellites abandoned in orbit is observed to be an important source of orbital debris. The operational life of satellites is typically short (just a few years). Once they are no longer operational, they effectively become debris if they remain in orbit. In most cases, satellites reach the end of their life after running out of fuel. Derelict satellites may still be functionally intact, but without fuel, they cannot be maneuvered to remain in their designated orbit. This means they lack maneuvering capacity. In such cases, they are abandoned in orbit, posing a risk of breakup due to residual fuel or battery explosions. In the early years of space exploration, the fraction of abandoned satellites was high. Over time, growing concerns about this practice have reduced the proportion of satellites left in orbit. Today, most spacefaring entities implement post-mission disposal (PMD) plans to either deorbit satellites or more them to a graveyard orbit at the end of their mission life.

This occurs when satellites exhaust their fuel reserves and can no longer be moved to graveyard orbits. Such cases were relatively common during the early stages of space exploration. Abandoned satellites pose a significant risk due to their size and mass. Indeed, one of the most damaging incidents was the collision between Kosmos 2251 with Iridium 33 in February 2009. However, the number of abandoned satellites is small compared to other types of orbital debris. Furthermore, new international standards for spacefaring nations and companies emphasize the importance of including reserve fuel for end-of-life deorbiting maneuvers. As a result, it is expected that the number of derelict satellites abandoned in orbit will decline over time, particularly as concerns about orbital debris continue to grow.

For the calibration of this parameter, we proceed as follows, using data from the ESA. As of December 2023, the total number of satellites launched is of 16,990, of which 11,500 remain in orbit. Hence, the difference $(16,990 - 11,500)$ corresponds to end-life satellites that have been deorbited, either naturally or intentionally, or have fragmented, totaling 5,490. In addition, the number of derelict satellites abandoned in orbit as of December 2023 is estimated at 3,500. Therefore, the total number of end-life satellites over the sample period, including the current stock of derelict satellites, amounts to $5,490 + 3,500 = 8,990$. Assuming that the accumulated number of derelict satellites corresponds to the number of abandoned end-life satellites, the lower bound for the fraction of satellites, the lower bound for the fraction of satellites abandoned in orbit can be approximated as: $\chi = 3,500/8,990 = 0.389$. Hence, we fix this parameter to be 0.4.

D.7 *Fraction of rocket bodies abandoned in orbit* (φ)

Rocket bodies represent another source of intact debris objects. Rocket bodies are large, with a substantial surface area and mass. Standard launch systems are composed of multi-stage rocket vehicles, typically two to four stages, to generate the necessary thrust to reach the target altitude. It is the upper stages of these rockets that are commonly left in orbit. Although some upper stages are brought back to Earth in a controlled manner, most are abandoned in orbit, as spacefaring agencies maximize the lifting capacity of rockets and typically do not reserve fuel for deorbiting maneuvers. Historically, not all launches have resulted in upper states remaining in orbit. This is primarily due to the NASA Space Shuttle program. NASA's shuttle fleet flew 135 missions, while the Soviet Union's Buran shuttle completed only one. Although the Space Shuttle developing reusable launch systems. For example, the SpaceX's Starship is not yet fully operational but has already completed four orbital test flights. On the other hand, some spacefaring operators systematically conduct upper stages disposal. For example, this is the case with SpaceX's Falcon-9 vehicles (a two-state rocket), where the second stage is deorbited after releasing its payloads. Jonathan McDowell's annual reports on Space Activities (the last one for the year 2024) provide detailed information about the disposal of launch vehicle upper stages. See also Byers and Boley (2023) and Wright et al. (2024) on this issue, who indicate that over 60% of launches to LEO resulted in at least one rocket body being abandoned in orbit. For the year 2018 (McDowell, 2019), the number of launches with upper stages disposal was of 33 out of 112, whereas the number of stages left in orbit was 89 out of 112 launches. Therefore, the ratio of abandoned rocket bodies in orbit to launches was of 0.795. The number of upper stages disposed of corresponds to the Falcom-9, SAST CZ-2D, and Vega-C vehicles. For the year 2019 (McDowell, 2020), the number of launches with upper stages disposal was 21, and the number of stages left in orbit was 86 out of 97, with a rocket body abandonment rate of 0.887. For 2020, there were 39 launches with upper stage disposal and 71 upper stages left in orbit out of 104 launches, resulting in an abandon rate of 0.683. According to Wright et al. (2024), in 2021, 97 out of 136 successful launches (71.3%) left rocket bodies in orbit. In 2022, the figure was 129 abandoned rocket bodies out of 180 launches, which represents a ratio of 71.7% (McDowell, 2023). For 2023, there were 122 rocket bodies abandoned from 212 successful launches, resulting in an abandonment rate of 57.5%, largely due to the high number of Falcon-9 launches, whose second stage are routinely deorbited (McDowell, 2024). Given this data, we adopt a baseline calibration of the model we used a value of $\phi = 0.60$, reflecting the recent trend in upper stages rocket body management.

D.8 *Fraction of dead satellites breakups (ε_w)*

A dead satellite abandoned in orbit is not only a big intact piece of debris, but also poses a significant risk of breaking up into thousands of fragments. The probability of such a breakup depends on several factors: the satellite's design, the presence of residual energy sources (such as unspent fuel or unpassivated batteries), and the duration of exposure to the harsh conditions of space, which deteriorate spacecraft components over time.

Accordingly to NASA's breakups database (Anz-Meador et al., 2022) a total of 47 satellite breakups had occurred by 2022, excluding deliberate destruction events. Of these, one involved an operational satellite, while the remaining 46 were derelict satellites. We estimate the value of this parameter by dividing the number of breakups by the estimated cumulative number of derelict satellites, W_t, calculated in Figure A.5. The cumulative number of derelict satellites for the period 1957-2023 is of 130,066. This gives a value of $46/130,066 = 0.00035$. In the baseline calibration of the model we use a value of $\delta_w = 0.001$.

D.9 *Fraction of rocket bodies breakups (ε_z)*

Rocket bodies (last stages of launch systems) contain engines and residual propellant tanks. As the rocket bodies spend extended periods in orbit, harsh environmental conditions can degrade their components, potentially causing explosions and fragmentation. These events are typically triggered by residual fuel, pressure changes in chemical tanks, or other physical and chemical processes. Kessler et al. (2010) indicate that in the initial years of space exploration, upper stages rocket bodies often tended to explode in orbit after a mission completion. However, since the early 1980's, design improvements and revised operational procedures have significantly reduced this risk.

According to NASA's monthly database on the number of objects in orbit, the number of rocket bodies as of December 2023 was 2,129. In NASA's breakups database (Anz-Meador et al., 2022), a total of 83 rocket body breakups have been recorded. The cumulative number of rockets launched is 6,508, and the cumulative number of rocket bodies abandoned in orbit over the full period is 70,282. Dividing the number of breakups by the total number of rocket bodies abandoned in orbit, we estimate that $\delta_z = 83/70,282 = 0.00118$.

D.10 *Number of fragments of debris per launch (ω)*

Launch activity is the primary source of debris generation, and the parameter ω represents the number of fragments generated per launch, excluding rocket bodies. This parameter includes only parts of launch vehicles discarded during the process of inserting a satellite into the target orbit, explicitly excluding expended rocket bodies. This is the case of payload fairings, connecting parts among rocket stages, adapter rings covers for optical instruments.

Jonathan McDowell's Space Activity reports offer detailed information on the number of debris pieces, excluding upper stages, released by launches for the years 2018 to 2023. According to this data, in 2018, there were 112 launches, producing 68 pieces of debris, approximately one piece for every two launches. In 2019, there were 97 launches and 38 pieces of debris. In 2020, 106 launches produced 61 debris pieces. In 2021, 136 launches resulted in 105 debris fragments. In 2022, 180 launches producing 143 pieces of debris. Finally, in 2023, 212 launches generated 61 debris items. Thus, over the 2019-2023 period, the number of debris pieces per launch remained below one, indicating a trend toward reduced debris generation during launch activities.

Lewis et al. (2009) estimated that an average of 2.75 intact objects are introduced into the space environment per launch. At a minimum, 2 fragments are released per launch, as payload fairings typically split into two halves, but additional objects are often expected to remain in orbit. Based on this, We assume that each launch produces a total of 4 fragments.

D.11 *Number of fragments per derelict satellites breakup* (ϕ_w)

Derelict satellites abandoned in orbit constitute intact objects that may breakup. These events occur when inactive satellites suddenly fragment due to explosions caused by residual fuel or ruptures in onboard batteries.

For the calibration of this parameter, we use information on recorded satellite breakups from Anz-Meador et al. (2022) and the DISCOS database. Some of these satellite breakups were intentional, such as several Soviet Union satellites that were deliberately destroyed.

In the NASA's brakups database (Anz-Meador et al., 2022), a total of 47 satellite breakups are recorded up to 2022, excluding deliberate destruction events (Table D.3). These breakups are mainly due to unknown causes (36 out of 47), although some of them could be associated with satellite inspectors (Killer satellites, such as the *Cosmos-252*, *Cosmos-375*, *and Cosmos-2535*) that, for unknown reasons, release debris when attacking the target satellite. In other cases, the confirmed cause is battery explosion (9 cases), and propulsion-related failures (2 cases).

TABLE D.3. Satellite breakups and cataloged debris. Source: Anz-Meador et al. (2022)

Cause	**Number**	**Cataloged debris**	**Cataloged debris per breakup**
Unknown	36	1,248	34.7
Battery	9	1,030	114.4
Propulsion	2	41	20.5
Total	47	2,319	49.3

The DISCOS database includes 12 fragmentation events involving satellites due to battery explosions, resulting in a total of 979 cataloged debris items (an average of 81.6 fragments per event). Additionally, there are three fragmentation events caused by accidental factors, which produced a total of 35 cataloged debris items, or approximately 11.7 fragments per event.

Another type of satellite fragmentation results from self-destruction using explosive charges, such as in the case of the *Cosmos-862* series. According to DISCOS, a total of 22 fragmentation events due to explosives are recorded, producing 173 cataloged fragments, which corresponds to an average of about 8 fragments per explosion.

D.12 *Number of fragments per rocket body breakup (ϕ_z)*

As with the previous parameter, we use the information from Anz-Meador et al. (2022) and the DISCOS database on rocket body breakup events and the corresponding number of debris generated. This database records a total of 83 rocket body breakups, resulting in 8,315 cataloged debris, which corresponds to an average of 100.2 fragments per event. The NASA database also includes ullage motor breakups, with 53 events producing 664 cataloged fragments, or 12.5 pieces per event. However, ullage motors are significantly smaller than standard rocket bodies and are no longer in use, making their contribution less relevant for current modeling purposes. Hence, we fixed $\phi_z = 100.2$.

Fragments resulting from the breakup of rocket bodies is highly dependent on the type of rocket. For example, according to DISCOS, the *Titan Transtage* experienced four breakup events, generating 194 cataloged fragments, for an average of 48,5 per breakup. In contrast, the Delta upper stage accounts for 15 breakups, producing a total of 1,959 cataloged debris, which represents an average of 130.6 fragments per event. The number of fragmentation events by *CZ-6A* recorded is of four, with an average number of 390.5 piece of debris fragments. For the *Ariane* rocket, a total of 30 breakups events, producing a total of 845 pieces of debris (an average of 28.3 debris fragments per event).

D.13 *Number of pieces of debris per operational satellite collision (γ_s)*

The number of new debris fragments generated by collisions between an operational satellite and a piece of orbital debris could vary significantly, primarily depending on the masses and relative velocities of the colliding objects. The most significant recorded incident occurred on 10 February 2009, involving the collision of an active US communications satellite (*Iridium-33*) with a defunct Russian satellite (*Kosmos-2251*). This event produced an estimated 2,371 cataloged debris fragments (Anz-Meador et al., 2022) while the ESA's DISCOS database lists 2,375 fragments for the same incident. In contrast, the collision involving *Sentinel-1A* resulted in only 9 cataloged fragments. However, this incident is not classified as a collision in the DISCOS database. The most recent recorded collision occurred 18 March 2021, when the Chinese satellite *Yunhai-1-02* collided with a piece of debris producing a total of 38 cataloged debris (37 according to DISCOS).

According to the NASA's breakups database (Anz-Meador et al., 2022), 7 confirmed collision events have been recorded to date, generating a total of 2,430 cataloged debris, averaging 347 fragments per collision. In addition, the database includes 67 events of unknown cause, which have produced 3,436 cataloged debris, averaging 51 pieces per event. According to the DISCOS database, a total of 6 fragmentation events due to collisions have been recorded. Five correspond to collision between operational satellites and pieces of orbital debris (*Cosmos-1934*, *Iridium-33*, *Cerise*, *Ayame-1*, and *Yunhai-1-02*). The sixth event corresponds to the collision of an upper stage motor (*Star-26B*) with a debris fragment on 17 January 2005, resulting in six cataloged debris fragments. When considering only the 5 events involving operational satellites, the average number of cataloged fragments per event is approximately 483.6.

On the other hand, a total of 51 deliberate self-destruction events, all attributed to Soviet Union satellites, are registered in the database. These events produced a combined 2,109 pieces of cataloged debris, yielding an average of 41 fragments per event. To estimate the total number of debris fragments larger than 1 cm, we extrapolate from the cataloged fragments (which represent objects larger than 10 cm) using the ratio of estimated debris: larger than 10 cm (36,500) and between 1 cm and 10 cm (1,000,000). The resulting figures are an average of 9,855 ($347 + 347 \times 27.4$) pieces of debris larger than 1 cm from collisions between operational satellites and debris, an average of 1,448 for the unknown events, and an average of 1,164 for self-destruction.

Farinella and Cordelli (1991) estimated this debris generation from hypervelocity impacts based on the typical mass distribution of fragments. Their findings suggest that a catastrophic collision, where the largest surviving fragment is around 10 kilograms, produces approximately 10,000 fragments with masses exceeding a few grams. Similarly, Lewis et al. (2009) found that the number of pieces of debris per catastrophic collision is 625 (collision with debris larger than 10 cm) and 25 for a damaging collision (collision with debris between 1 and 10 cm). Applying the scaling factor used to estimate debris larger than 1 cm, the results is 17,750 for catastrophic collision and 710 in the case of a non-catastrophic collision. The NASA Standard Breakup model further refines these estimates by modeling fragments production based on mass and energy transfer in collisions, calibrated through laboratory hypervelocity impact experiments. Jonhson et al. (2001) found similar outcomes between two objects with a combined mass of of 1,260 kg, which is comparable to the average mass of a medium-class satellite (Bryce, 2020). Assuming a uniform collision probability across debris size classes, the final calibrated estimate for the number of fragments larger than 1 cm per collision event is 1,309, a figure closely aligned with those derived from observed accidental explosions. Based on all previous information, we fixed $\gamma_s = 70$ as the baseline.

D.14 *Number of fragments from derelict satellites collision (γ_w)*

Derelict satellites are non-operational satellites that have reached the end of their service life (i.e., have run out of fuel) and remain in orbit without any form of control. These uncontrolled objects pose a collision risk to both operational satellites and other pieces of orbital debris. The only registered collision involving a derelict satellite was a collision with an operational satellite (the collision of the derelict satellite *Cosmos-2251* with the operational satellite *Iridium-33*). Anz-Meador et al. (2002) indicate that this collision produced a total of 2,371 cataloged fragments. However, this collision involved two large objects, and we can expect a lower number of fragments in the case of collision with a small piece of debris.

Although data is limited, derelict satellites have the same characteristics as operational satellites. Therefore, in case of collision, we can argue that they will be fragmented in a similar way to the rest of the operational satellites. This means that the calibration of the parameter γ_w takes the same value as the parameter γ_s, although the model allows for using a different fragmentation coefficient than that of operational satellites. Therefore, we fix $\gamma_w = 70$.

D.15 *Number of fragments from rocket bodies collision (γ_z)*

Given the differences in mass and size between rocket bodies and satellites, we might expect a different fragmentation behavior in the event of a collision between these two types of objects. Kessler et al. (2010) indicate that, whereas a number of tests have been conducted to understand the size distribution from the collision of a payload, none have been conducted on rocket bodies, and the standard assumption in breakups models is that payloads and rocket bodies fragment under identical conditions and produce identical fragment distribution. However, as Kessler et al. (2010) point out, the large tank of rocket bodies may not absorb all the energy of a collision, or, by contrast, could dissipate the energy of a collision over the opposite tank wall, acting like a Whipple shield. Therefore, it remains unclear whether a rocket body collision would generate more fragments or fewer fragments than a satellite collision.

The source for the calibration of this parameter is Anz-Meador et al. (2022). However, there is only one collision in January 2005 between a rocket body (*DMSP-5B-F5 Thor-Burner 2A rocket*) and other debris from a Chinese ASAT test, producing 5 cataloged debris fragments. Another collision was deliberate (the collision of USA-19 with the upper stage of USA-19), resulting in the fragmentation of USA-19 in 13 cataloged debris fragments and the fragmentation of the rocket body into 5 cataloged debris fragments. Given the lack of available data, we adopt the same assumption as the LEGEND model: that both payloads and rocket bodies produce identical fragment distributions in case of collision. Therefore, we assume that $\gamma_z = 70$.

There is more extensive data available from upper stage explosions in orbit (parameter ε_z). As noted by Kessler et al. (2010), collisions release significantly more energy than explosions, and thus we would expect the number of fragments produced by a collision to be larger than that the produced by an explosion. Previously, the parameter representing cataloged fragments from rocket bodies breakups was estimated to be 100, based on the information from the NASA breakups database, which is larger than the number of fragments produced by satellite breakups. However, based on the Kessler et al. (2010) arguments, we take a conservative perspective, and assume a number of fragments from rocket bodies collisions as for derelict satellites collisions.

D.16 *Collision avoidance fraction (v_t)*

The damage function incorporates an additional variable to account for collision avoidance operations. Operational satellites, except for small cubsats in LEO, are capable of performing maneuvers to prevent collisions. When such maneuvers are successfully executed, collisions, and the resulting destruction of the satellite, are avoided, thereby preventing the generation of debris fragments that would otherwise occur. This variable is assumed to be determined exogenously. In the baseline scenario, the fraction of avoided collisions is set to zero. In the no-collision scenario, the value of v_t is set to one. However, the model can be simulated for any value of the collision avoidance fraction up to one. Alternatively, v_t can be modeled as a time-varying, increasing function, which could be justified by technological advancements in tracking orbiting objects, improved conjunction assessments, and enhanced spacecraft maneuverability. This is left for a future extension of the model.

D.17 *Size debris proportional parameter*

The model considers different types of debris depending on their size, following standard classification by the ESA: debris between 1 mm and 1 cm, debris between 1 cm and 10 cm, and debris larger than 10 cm. Whereas DISE-2024 consider that debris larger than 1 cm can be catastrophic in case of collision, for the calibration of the different parameters of the model, available information refers to tracked or cataloged debris, which usually have larger than 10 cm in size. Therefore, whereas the debris module calculates debris larger than 10 cm, the collision probability and the damage functions require the population of debris larger than 1 cm.

Mains et al. (2024) use the IMPACT satellite fragmentation model (Mains and Sorge, 2022) to study four fragmentation events, including two collision (*Cosmos- 1408* ASAT test and *SL-14* rocket body), a rocket body breakup (*Long March 6A*), and a satellite breakup (*Resur-01*). The IMPACT model is used to predict the number of fragments larger than 10 cm and larger than 1 cm. A summary of the results is shown in Table D.4, including the number of cataloged objects and the estimated number of fragments larger than 10 cm and 1 cm. The average proportion across the three events is 63.21. Nevertheless, this is a limited sample, and difficult to extrapolate to the whole debris environment.

TABLE D.4. IMPACT model estimations

Object	Cataloged	Fragments > 10 cm	Fragments > 1 cm	Ratio
Cosmos-1408	1,600	1,320	200,000	151.50
CZ-6A R/B	500	734	20,000	27.24
Resur-01	100	147	1,600	10.88
Average	*733.33*	*733.66*	*73,866.66*	*63.21*

Source: Mains et al. (2024).

Based on the population of debris of different sizes estimated by the ESA, to compute the number of debris larger than 1 cm, we use the scaling factor as follows,

$$\Gamma = \frac{1,000,000}{(36,500 - 2,050 - 3,500)} = 32.3 \tag{D.10}$$

where 1 million is the population of debris between 1 cm and 10 cm at December 2023 estimated by the ESA, 36,500 is the population of debris larger than 10 cm by ESA, 2,050 is the number of rocket bodies and 3,500 the number of derelict satellites.

APPENDIX E: EXOGENOUS SOURCES OF GROWTH

The economy module of DISE-2024 incorporates three exogenous sources of growth: Two types of technological progress, one aggregate and other specific to the space sector, and world population (i.e., labor) growth. The assumptions about these processes remain key, as economic growth is the main determinant of the space environment. Table E.1 shows the selected values for the parameters of the processes for TFP, satellite-ISTC, and population growth.

TABLE E.1. Baseline calibration of exogenous sources of growth of DISE-2024

Parameter	**Definition**	**Value**	**Source**
g_a	TFP growth rate	0.015	Assumption
g_q	Satellite ISTC growth rate	0.030	Assumption
δ_a	TFP growth decay rate	0.001	Assumption
δ_q	ISTC growth decay rate	0.005	Assumption
ς	Population growth parameter	0.05	Assumption

E.1 *Total Factor Productivity (a_t)*

At is standard in growth models, aggregate technical progress is represented by a Hicks-neutral technological change. This is an important sources of output growth. We assume that Total Factor Productivity (TFP) follows an exogenous process defined as follows,

$$a_{t+1} = exp(g_{a,t})a_t \tag{E.1}$$

where $g_{a,t}$ is the growth rate of TFP defined as,

$$g_{a,t} = g_{a,0}exp(-\delta_a t) \tag{E.2}$$

where $g_{a,0}$ is the TFP growth rate in the base period ($t = 0$, which corresponds to the year 2023) and δ_a is the decay rate of the TFP growth rate.

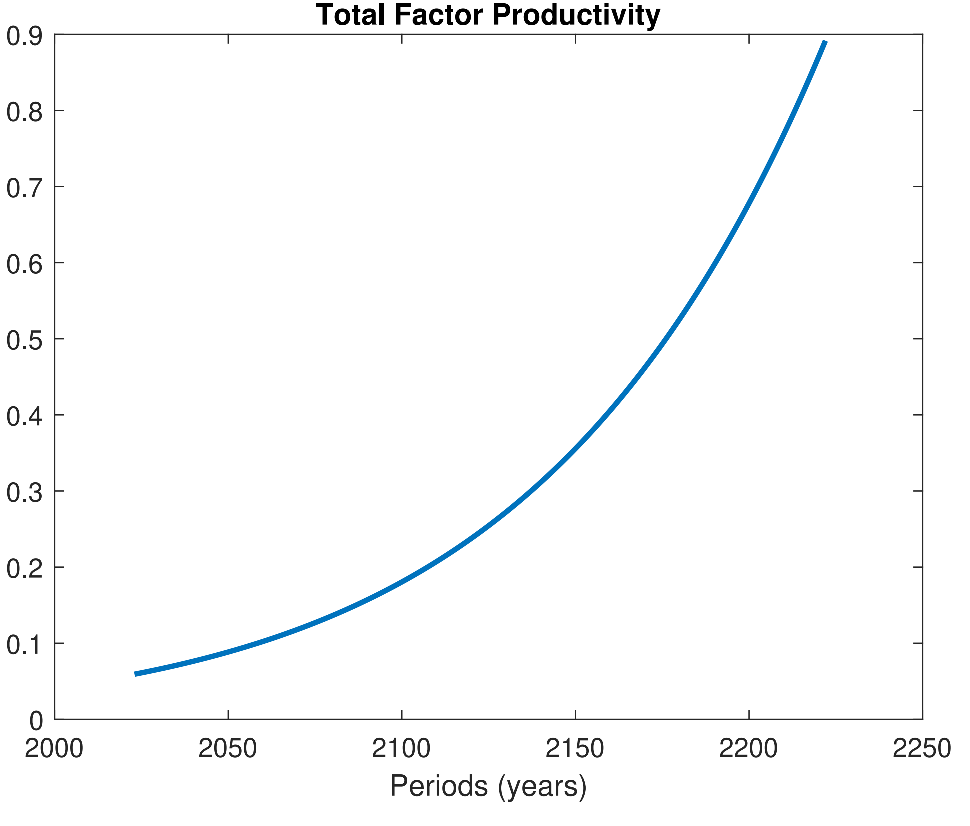

FIGURE E.1. Total Factor Productivity

Initial value for TFP is calculated as:

$$a_{2023} = \frac{y_{2023}}{k_{2023}^{\alpha_1} s_{2023}^{\alpha_2} N_{2023}^{1-\alpha_1-\alpha_2}} = \frac{184.65}{552.474^{0.3479} 1.203^{0.0021} 8,056^{0.65}} = 0.0593. \tag{E.3}$$

We assume an initial TFP growth rate of 1.5% per year, with a decay rate in the growth rate of 0.1% per year. For comparison, DICE-2023 assumes an initial TFP growth of 0.066 (per 5 years), with a decline rate of 0.0015 (per 5 years). Roughly, this is equivalent to an initial annual TFP growth rate of 0.0132, and a decline rate of 0.003, values which are similar to the ones used in DISE-2024.

Figure E.1 plots the time path of TFP over the simulation horizon. Although TFP growth rate is decreasing (Figure E.2), the accumulation process results in an exponential path.

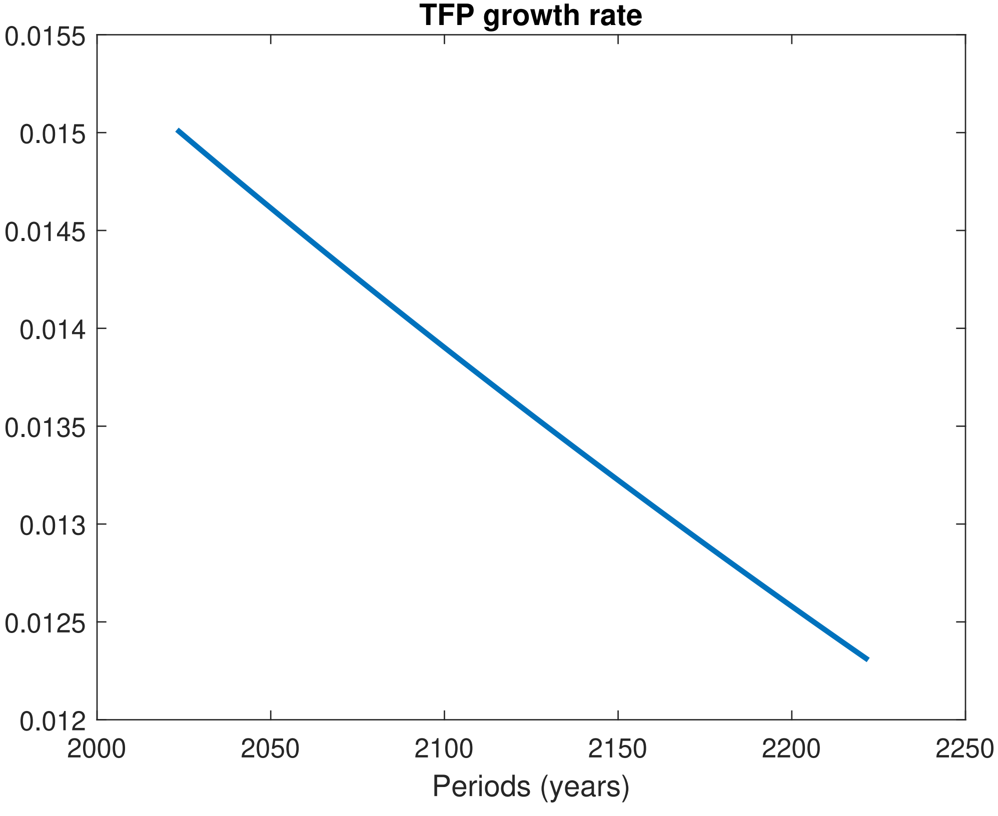

FIGURE E.2. Growth rate of Total Factor Productivity

E.2 *Satellite investment-specific technological change* (q_t)

In the model economy represented by DISE-2024, technological change is not only captured by a Hicks neutral technological change through TFP, but also by embodied-technological progress. We consider an additional form of technological progress specific to satellites, following Greenwood, Hercowitz and Krusell (1997). Greenwood et al. (1997) introduce ISTC in a growth model with two capital assets: structures and equipment, where ISTC applies to equipment. DISE-2024 incorporates ISCT for space capital, reflecting the assumption that space assets will experience a higher rate of technological progress compared to Earth capital assets. This is equivalent to assuming that the price of space assets will decline in the future at a faster rate than the prices of Earth capital assets.

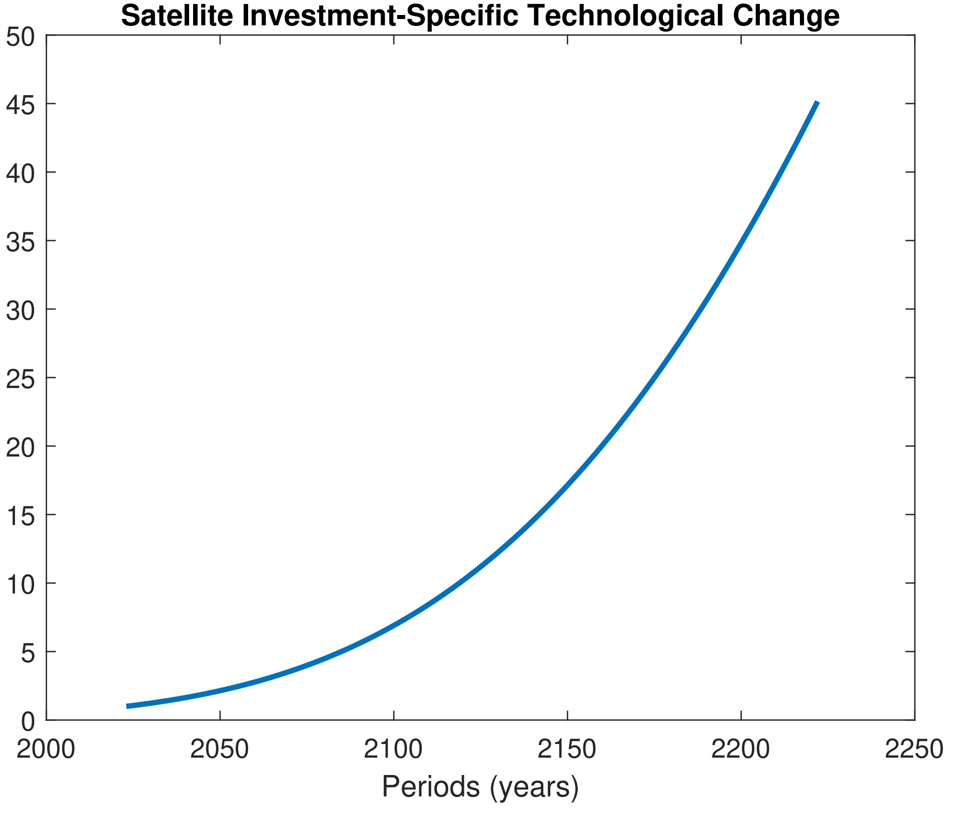

FIGURE E.3. Satellite Investment-Specific Technological Change

Similarly to TFP, we assume that ISTC follows an exogenous process given by,

$$q_{t+1} = exp(g_{q,t})q_t \tag{E.4}$$

where $g_{q,t}$ is the growth rate of ISTC defined as,

$$g_{q,t} = g_{q,0} exp(-\delta_q t) \tag{E.5}$$

where $g_{q,0}$ is the ISTC growth rate in the base period and δ_q is the decay rate of the TFP growth rate.

Initial value for ISTC is normalized to one ($q_{2023} = 1$). It is assumed that the initial growth rate of ISTC is 3% ($g_{q,0} = 0.03$), where the growth rate decays at 0.5% ($\delta_q = 0.05$). Results are plotted in figures E.3 and E.4.

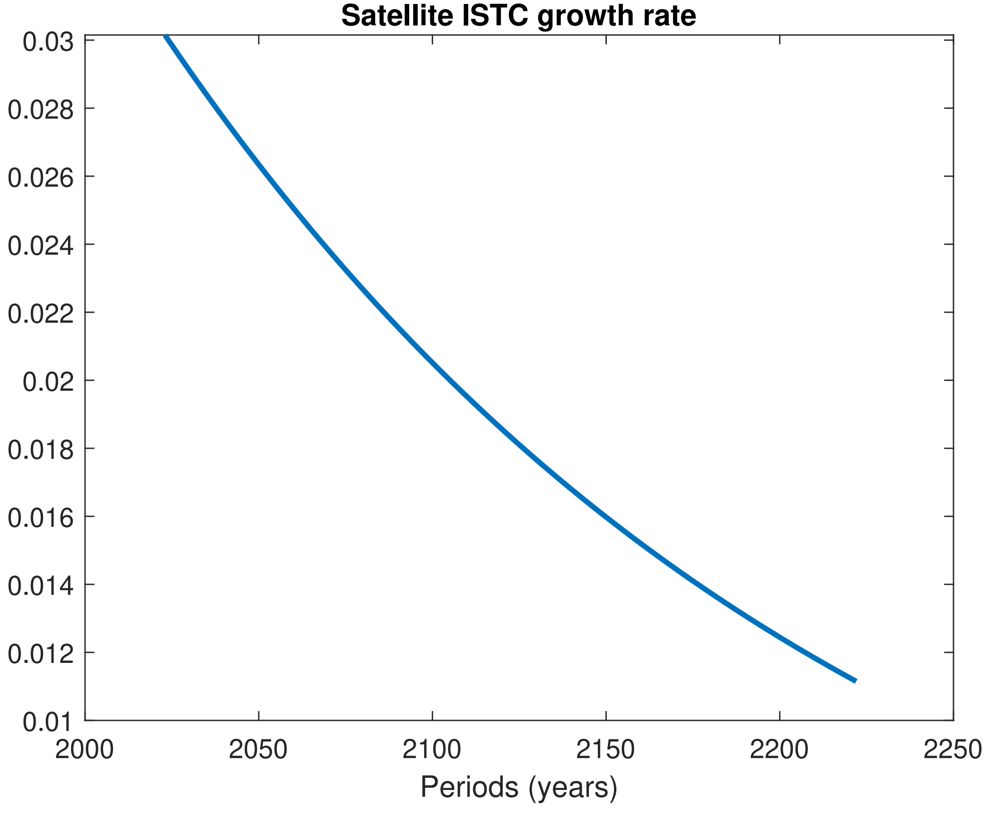

FIGURE E.4. Growth rate of satellite ISTC

E.3 *Population (N_t)*

Another source of economic growth is population growth. This is because production input labor is assumed to be equal or proportional to population. Hence, population is an additional production factor to Earth capital and space capital, and output growth is a function of population growth. In DISE-2024, we use data from World Population Prospects 2024 (UN, 2024) which includes projections to the year 2100. Using those projections, we extend population to the year 2222 assuming that from 2100 onward population growth is almost zero. The base year (2023) for the world population is 8,056,505 thousand. The asymptotic population is 10,200 million (see Figure E.5). Population contributes to output growth until approximately the year 2100, being zero for the last years of the simulation period.

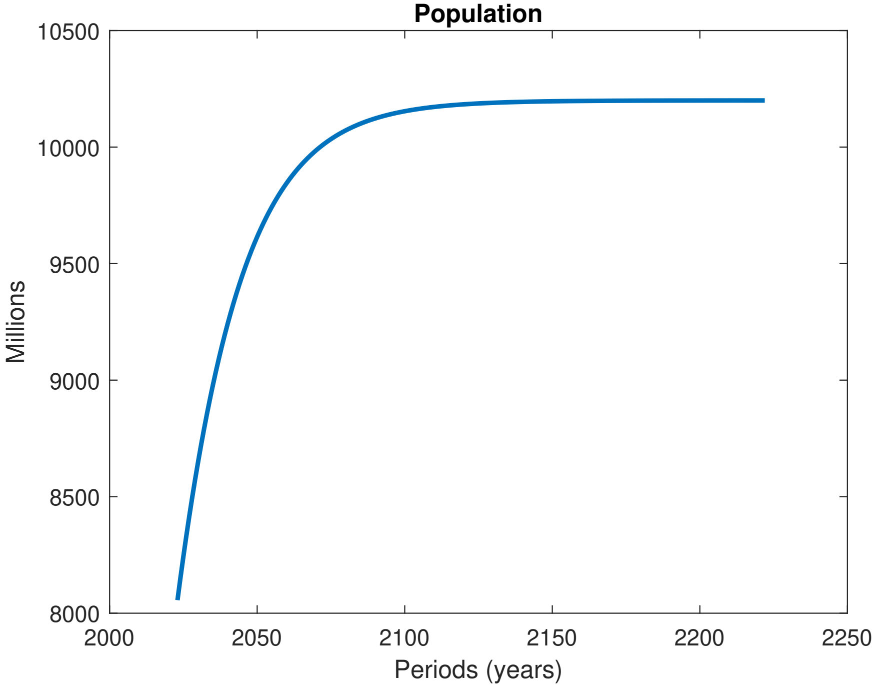

FIGURE E.5. Population projections. Based on World Population Prospects 2024, Medium fertility variant, 2024-2100, extended to 2222.

Formally, world population is calculated as,

$$N_{t+1} = N_t \left(\frac{N^*}{N_t} \right)^{\varsigma} \tag{E.6}$$

where N^* is an asymptotic population and the parameter ς is a parameter driving the growth rate of population to the asymptotic population. Initial growth rate is around 1.2%, decreasing to zero by the year 2150 (Figure E.6).

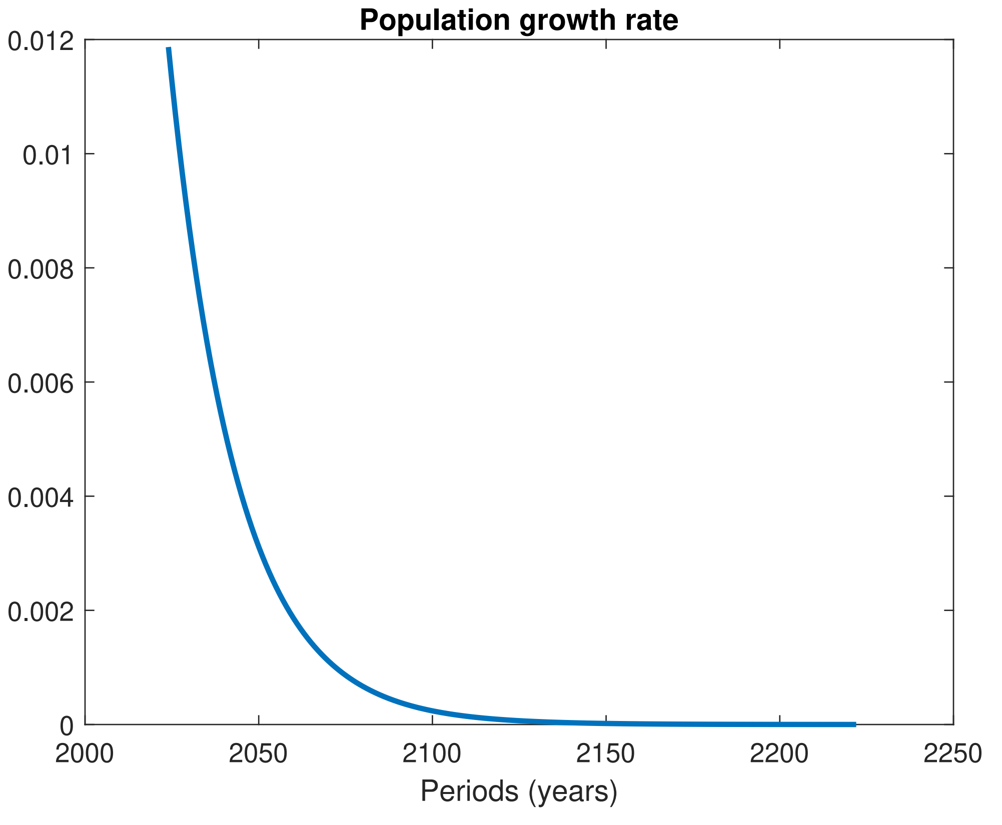

FIGURE E.6. World population growth rate

E.4 *GDP growth*

As shown previously, the model has three exogenous sources of growth: neutral technological change, satellite ISTC, and population (employment) growth, and two endogenous sources of growth: accumulation of Earth and space capital. To show how calibration of these exogenous process affects output growth, we simulate the model in a sci-fi scenario with no orbital debris. Figure E.7 plots the result of the output growth in the simulation horizon for the clean space environment scenario. It can be seen that the initial output growth is around 3%, which decreases to less than 2% at the end of the simulation period.

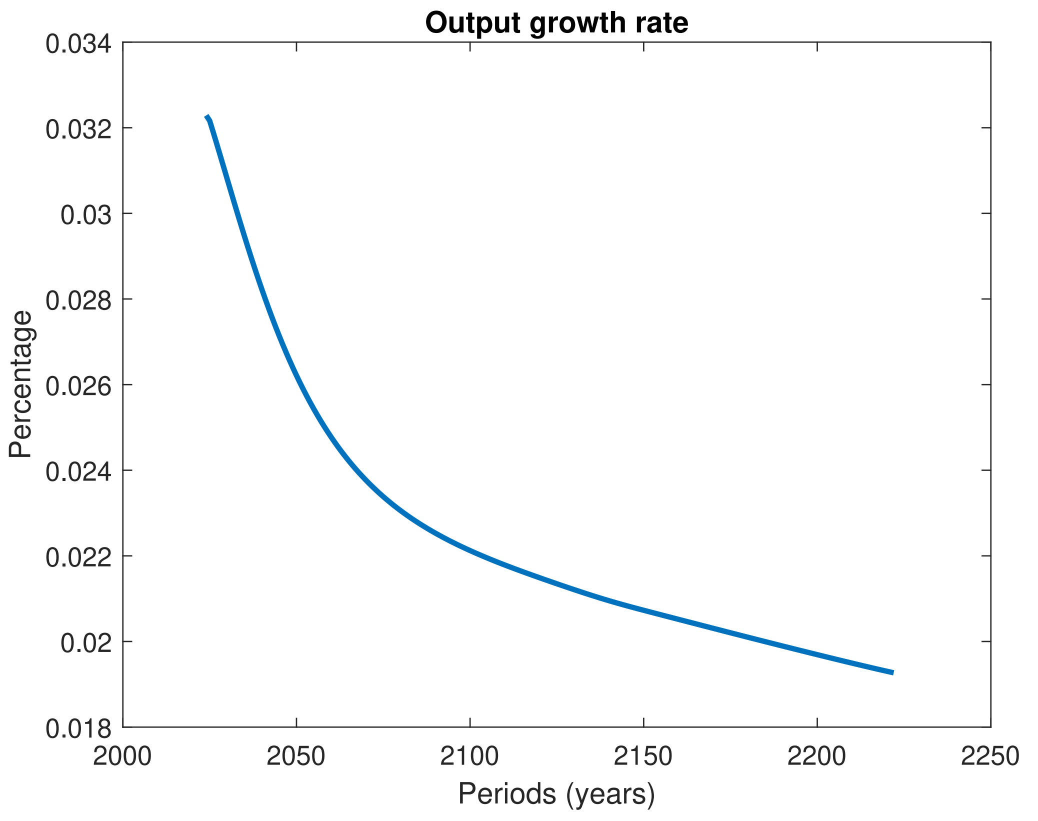

FIGURE E.7. GDP growth rate

APPENDIX F: LAUNCH COST

When computing investment in space capital, the model takes into account the existence of an installation cost, i.e., and investment adjustment cost to effectively accumulate investment into space capital. This installation cost is represented by launch costs. Making operational a satellite, even if the satellite is completed manufactured, is not a direct process, as the satellite have to be moved from the Earth to outer space. For inserting a satellite in orbit, it is necessary a launch vehicle, which is costly. This means that a fraction of investment in space capital is loss in the process of installation of the satellite into orbit. The model assumes that the launch cost is a constant fraction of the total investment cost and that the initial launch cost is 30% ($m_0 = 0.3$) of total investment in space capital, and hence, only the 70% of gross investment accumulates into satellite assets. This cost, together with a high depreciation rate, result in a high rate of return of satellites. In the baseline, we assume that launch cost is constant ($g_{m,t} = 0$).

The model also assumes that the launch cost is decreasing over time. Adilov et al. (2022) estimate that from 2000 to 2020 the per-kilogram launch costs decreased at an average annual rate of 5.5% (a 4.4% if altitude-adjusted). Adilov et al. (2022) report that between 2000 and 2020, launch costs per kilogram to low Earth orbit declined significantly, driven by decreasing satellite masses, with projections indicating they will drop below \$1000/kg between 2045–2076 and \$100/kg by the next century.

For simulating the trajectory of the fraction of the launch cost, we use the following specification,

$$m_{t+1} = exp(g_{m,t})m_t \tag{F.1}$$

where $g_{m,t}$ is the (negative) growth rate of launch cost,

$$g_{m,t} = g_{m,0}exp(-\delta_m t) \tag{F.2}$$

where $g_{m,0}$ is the change in launch cost in the base year and δ_m is the decay rate of the change in launch cost.

Figure F.1 plots the fraction of launch cost over total investment in space capital, reflecting a decline in the launch cost, as a fraction of total cost, over time. Following estimates by Adilov et al. (2022), we assume that the initial decline in launch cost is of 5% ($g_{m,0} = -0.05$), and that the decline in the growth rate is of 1% ($\delta_m = 0.01$). Based on that figures, the fraction of launch cost reduces to 15% of total cost by 2050, and to only 5% by about 2100. The decreasing launch cost can be justified by a number of factors, including learning-by-doing process in the launching industry, technological progress in launch vehicles, reduction in the size and mass of satellites, and commercial use of low altitude orbits.

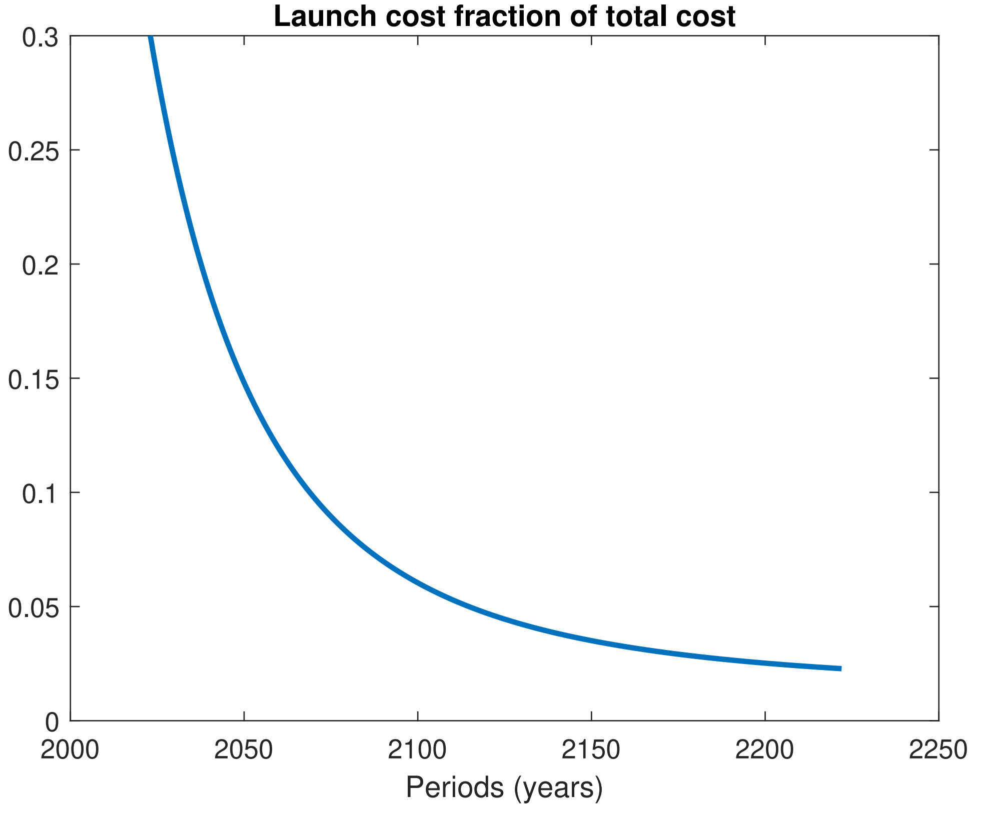

FIGURE F.1. Fraction of launch cost over total cost of space capital investment

Appendix G: The model

This appendix collects the equations of the DISE-2024 model. The economic sub-model is formed by the following equations:

$$max_{\{c_t\}_{t=0}^{\infty}} \sum_{t=0}^{\infty} \left(\frac{1}{1+\rho}\right)^t U(\hat{c}_t, N_t) \tag{G.1}$$

$$c_t + i_t^k + i_t^s = y_t \tag{G.2}$$

$$y_t = a_t f(k_t, s_t, N_t) \tag{G.3}$$

$$k_{t+1} = (1-\delta_k)k_t + i_t^k \tag{G.4}$$

$$i_t^s = h_t + l_t \tag{G.5}$$

$$l_t = m_t i_t^s \tag{G.6}$$

$$s_{t+1} = (1-\delta_s)s_t + q_t h_t - x_t \tag{G.7}$$

The damage function linking the economic sub-model with the debris sub-model is the following,

$$x_t = (1-v_t)\theta D_{2,t} s_t \tag{G.8}$$

The debris sub-model is given by,

$$D_{i,t} = W_t + B_t + F_{i,t} \qquad i = 1,2,3 \tag{G.9}$$

$$W_{t+1} = (1-\delta_w-\varepsilon_w)W_t - \theta(D_{2,t} + (1-v_t)S_t)W_t + \chi\delta_s S_t \tag{G.10}$$

$$Z_{t+1} = (1-\delta_z-\varepsilon_z)Z_t - \theta(D_{2,t} + (1-v_t)S_t)Z_t + \varphi L_t \tag{G.11}$$

$$\begin{aligned} F_{1,t+1} = (1-\delta_f)F_{1,t} + \omega L_t + \phi_w\varepsilon_w W_t + \phi_z\varepsilon_z Z_t + \\ \gamma_s X_t + \gamma_w\theta D_{2,t} W_t + \gamma_z\theta D_{2,t} Z_t \end{aligned} \tag{G.12}$$

The mapping between economic and physical variables is given by,

$$S_t = \frac{\mu s_t}{q_t} \tag{G.13}$$

$$X_t = \frac{\mu x_t}{q_t} \tag{G.14}$$

$$H_t = \mu h_t \tag{G.15}$$

$$S_{t+1} = (1 - \delta_s) S_t + H_t - X_t \tag{G.16}$$

$$X_t = (1 - v_t)\theta D_{2,t} S_t \tag{G.17}$$

The launch sub-module is composed by the following equations:

$$H_t = \eta L_t \tag{G.18}$$

$$h_t = (1 - b_t) i_t^s = \frac{\eta}{\mu q_t} L_t \tag{G.19}$$

Exogenous sources of growth are:

$$a_{t+1} = exp(g_{a,t}) a_t \tag{G.20}$$

$$g_{a,t} = g_{a,0} exp(-\delta_a t) \tag{G.21}$$

$$q_{t+1} = exp(g_{q,t}) q_t \tag{G.22}$$

$$g_{q,t} = g_{q,0} exp(-\delta_q t) \tag{G.23}$$

$$N_{t+1} = N_t \left(\frac{N^*}{N_t} \right)^{\varsigma} \tag{G.24}$$

Finally, the cost of launches is given by,

$$m_{t+1} = exp(g_{m,t}) m_t \tag{G.25}$$

$$g_{m,t} = g_{m,0} exp(-\delta_m t) \tag{G.26}$$

G.1 *Decentralized economy (Laissez-faire)*

Although we do not simulate the model for a decentralized economy, it is nevertheless interesting to calculate the optimal investment decisions on Earth and space capital by households. In a decentralized economy, the negative externality of orbital debris is not internalized. Agents simply adapt to the space environment, treating the amount of orbital debris is considered exogenous. The household maximization problem, taking into account the accumulation process for both capital and satellites, is given by,

$$\mathcal{L} = E_0 \sum_{t=0}^{\infty} \beta^t U(\hat{c}_t) N_t$$

$$-\sum_{t=0}^{\infty}\lambda_t[c_t+k_{t+1}-(1-\delta_k)k_t+\frac{1}{q_t(1-m_t)}[s_{t+1}-(1-\delta_s)s_t+(1-v_t)\theta\overline{D}_{2,t}s_t] \\ -r_t^k k_t - r_t^s s_t - \pi_t] \quad (G.27)$$

where $\overline{D}_{2,t}$ is the exogenous amount of orbital debris.

First order conditions from $t = 0, 1, ..., \infty$, are:

$$\frac{\partial \mathcal{L}}{\partial c_t} = \beta^t U'(c_t) - \lambda_t = 0 \quad (G.28)$$

$$\frac{\partial \mathcal{L}}{\partial k_{t+1}} = -\lambda_t + \lambda_{t+1}(1-\delta_k + r_{t+1}^k) \quad (G.29)$$

$$\frac{\partial \mathcal{L}}{\partial s_{t+1}} = \frac{\lambda_t}{q_t(1-m_t)} - \frac{\lambda_{t+1}}{q_{t+1}(1-m_{t+1})}[1-\delta_s-(1-v_t)\theta\overline{D}_{2,t+1}] + \lambda_{t+1}r_{+1}^s = 0 \quad (G.30)$$

From the maximization problem, solving for the Lagrangian's multiplier, equilibrium conditions are given by,

$$U'(c_t) = \beta E_t U'(c_{t+1})[1-\delta_k + r_{t+1}^k] \quad (G.31)$$

$$U'(c_t) = q_t(1-m_t)\beta E_t U'(c_{t+1})\left[\frac{1-\delta_s-(1-v_t)\theta\overline{D}_{2,t+1}}{q_{t+1}(1-m_{t+1})} + r_{t+1}^s\right] \quad (G.32)$$

Expression (G.31) is the standard Euler equation for optimal investment decisions in capital excluding satellites. Expression (G.32) is also an Euler equation, but it pertains to the investment decision in satellites, where the cost of destruction by collision is incorporated. The term $\theta\overline{D}_{t+1}$ accounts for the sudden, full depreciation of satellites stock due to collisions. As the quantity of orbital debris increases, the rental price of satellite to capital also increases.

The representative firm maximizes profits by choosing the appropriate levels of capital and satellites. Profits are defined as,

$$\pi_t = y_t - r_t^k k_t - r_t^s s_t \quad (G.33)$$

From the profit maximization problem we have:

$$r_t^k = a_t f_k'(k_t, s_t) \quad (G.34)$$

$$r_t^s = a_t f_s'(k_t, s_t) \quad (G.35)$$

Equilibrium conditions are obtained by substituting (G.34) and (G.35) into (G.31) and (G.32),

$$U'(c_t) = \beta E_t U'(c_{t+1})[1 - \delta_k + a_{t+1} f_k'(k_{t+1}, s_{t+1})] \tag{G.36}$$

$$U'(c_t) = q_t(1 - m_t)\beta E_t U'(c_{t+1}) \left[\frac{1 - \delta_s - (1 - v_t)\theta \overline{D}_{2,t+1}}{q_{t+1}(1 - m_{t+1})} + a_{t+1} f_s'(k_{t+1}, s_{t+1}) \right] \tag{G.37}$$

Equating both expressions we find that the arbitrage condition for investing in both Earth and space capital is,

$$[1 - \delta_k + a_{t+1} f_k'(k_{t+1}, s_{t+1})] = q_t(1 - m_t) \left[\frac{1 - \delta_s - (1 - v_t)\theta \overline{D}_{2,t+1}}{q_{t+1}(1 - m_{t+1})} + a_{t+1} f_s'(k_{t+1}, s_{t+1}) \right] \tag{G.38}$$

G.2 *Centralized economy*

This section sets out the planning problem in which a central planner seeks to maximize social welfare. The planner determines the optimal allocation of consumption, investment in terrestrial capital, investment in satellite capital, and orbital debris. This corresponds to the first-best outcome, wherein the negative externality is fully internalized. The central planner's optimization problem can be expressed as:

$$\max_{c_t, i_t^k, i_t^s, D_t} E_0 \sum_{t=0}^{\infty} \beta^t U(\hat{c}_t) N_t \tag{G.39}$$

subject to

$$c_t + i_t^k + i_t^s = y_t \tag{G.40}$$

$$y_t = a_t f(k_t, s_t, N_t) \tag{G.41}$$

$$k_{t+1} = (1 - \delta_k)k_t + i_t^k \tag{G.42}$$

$$i_t^s = h_t + l_t \tag{G.43}$$

$$l_t = m_t i_t^s \tag{G.44}$$

$$s_{t+1} = (1 - \delta_s)s_t + q_t(1 - m_t)i_t^s - x_t \tag{G.45}$$

$$x_t = (1 - v_t)\theta D_{2,t} s_t \tag{G.46}$$

$$D_{i,t} = W_t + Z_t + F_{i,t} \qquad i = 1, 2, 3 \tag{G.47}$$

$$W_{t+1} = (1 - \delta_w - \varepsilon_w)W_t - \theta(Z_t + F_{2,t} + (1 - v_t)S_t)W_t + -\theta \frac{S_t^2}{2} \chi \delta_s S_t \tag{G.48}$$

$$Z_{t+1} = (1-\delta_z-\varepsilon_z)Z_t - \theta(W_t + F_{2,t} + (1-v_t)S_t)Z_t - \theta\frac{Z_t^2}{2} + \varphi L_t \tag{G.49}$$

$$F_{1,t+1} = (1-\delta_f)F_{1,t} + \omega L_t + \phi_w\varepsilon_w W_t + \phi_z\varepsilon_z Z_t +$$

$$\gamma_s X_t + \gamma_w\theta(Z_t + F_{2,t})W_t + \gamma_w\theta\frac{W_t^2}{2} + \gamma_z\theta(W_t + F_{2,t})Z_t + \gamma_z\theta\frac{W_t^2}{2} \tag{G.50}$$

$$L_t = \frac{\mu}{\eta}h_t \tag{G.51}$$

$$X_t = \mu\frac{x_t}{q_t} \tag{G.52}$$

$$F_{2,t} = (1+\Gamma)F_{1,t} \tag{G.53}$$

Additionally, the mapping from the "economic" model to the "physical" model is given by the following expressions:

$$X_t = (1-v_t)\theta D_{2,t}S_t \tag{G.54}$$

$$S_t = \mu\frac{s_t}{q_t} \tag{G.55}$$

$$H_t = \eta L_t \tag{G.56}$$

The maximization problem can be defined as:

$$\begin{aligned}
\mathcal{L} = E_t\sum_{t=0}^{\infty}\beta^t U(\hat{c}_t)N_t \\
-\sum_{t=0}^{\infty}\lambda_{1,t}\left[c_t + k_{t+1} - (1-\delta_k)k_t + \frac{\eta}{\mu(1-m_t)}L_t - a_t f(k_t, s_t, N_t)\right] \\
-\sum_{t=0}^{\infty}\lambda_{2,t}\left[x_t - (1-v_t)\theta D_{2,t}s_t\right] \\
-\sum_{t=0}^{\infty}\lambda_{3,t}\left[s_{t+1} - (1-\delta_s)s_t - \frac{\eta}{\mu}q_t L_t + x_t\right] \\
-\sum_{t=0}^{\infty}\lambda_{4,t}\left[D_{2,t} - W_t - Z_t - (1+\Gamma)F_{1,t}\right] \\
-\sum_{t=0}^{\infty}\lambda_{5,t}[W_{t+1} - (1-\delta_w-\varepsilon_w)W_t + \theta(Z_t + F_{2,t} + (1-v_t)S_t)W_t + \theta\frac{W_t^2}{2} - \chi\delta_s S_t] \\
-\sum_{t=0}^{\infty}\lambda_{6,t}[Z_{t+1} - (1-\delta_z-\varepsilon_z)Z_t + \theta(W_t + F_{2,t} + (1-v_t)S_t)Z_t + \theta\frac{Z_t^2}{2} - \varphi L_t] \\
-\sum_{t=0}^{\infty}\lambda_{7,t}[F_{1,t+1} - (1-\delta_f)F_{1,t} - \omega L_t - \phi_w\varepsilon_w W_t - \phi_z\varepsilon_z Z_t
\end{aligned}$$

$$-\gamma_s X_t - \gamma_w \theta D_{2,t} W_t - \gamma_z \theta D_{2,t} Z_t - \gamma_w \theta \frac{W_t^2}{2} - \gamma_z \theta \frac{Z_t^2}{2}] \tag{G.57}$$

The Lagrangian multipliers for each constraint in period t are $\lambda_{1,t}$, $\lambda_{2,t}$, $\lambda_{3,t}$, $\lambda_{4,t}$, $\lambda_{5,t}$, $\lambda_{6,t}$, and $\lambda_{7,t}$. $\lambda_{1,t}$ is the standard shadow price of consumption. $\lambda_{2,t}$ is the cost of the probability of collision. $\lambda_{3,t}$ is the price of satellite assets. $\lambda_{4,t}$ is the cost of the stock of orbital debris, and $\lambda_{5,t}$, $\lambda_{6,t}$, and $\lambda_{7,t}$ represents the shadow cost of derelict satellites, rocket bodies, and fragments, respectively.

First order conditions from the maximization problem, for $t = 0, 1, ..., \infty$ are,

$$\frac{\partial \mathcal{L}}{\partial c_t} = \beta^t U'(c_t) - \lambda_{1,t} = 0 \tag{G.58}$$

$$\frac{\partial \mathcal{L}}{\partial k_{t+1}} = -\lambda_{1,t} + \lambda_{1,t+1}\left[1 - \delta_k + a_{t+1} f_k'(k_{t+1}, s_{t+1}, N_{t+1})\right] = 0 \tag{G.59}$$

$$\begin{aligned}\frac{\partial \mathcal{L}}{\partial s_{t+1}} &= \lambda_{1,t+1} a_{t+1} f_s'(k_{t+1}, s_{t+1}, N_{t+1}) + \lambda_{2,t}(1 - v_t)\theta D_{2,t+1} - \lambda_{3,t} + \lambda_{3,t+1}(1 - \delta_s) \\ &\quad -\lambda_{5,t+1}\frac{\mu}{q_{+1}}[\theta(1 - v_{t+1})W_{t+1} - \chi\delta_s] - \lambda_{6,t+1}\frac{\mu\theta(1 - v_{t+1})Z_{t+1}}{q_{t+1}} = 0\end{aligned} \tag{G.60}$$

$$\frac{\partial \mathcal{L}}{\partial L_t} = -\lambda_{1,t}\frac{\eta}{\mu(1 - m_t)} + \lambda_{3,t}\frac{\eta q_t}{\mu} + \lambda_{6,t}\varphi + \lambda_{7,t}\omega = 0 \tag{G.61}$$

$$\frac{\partial \mathcal{L}}{\partial x_t} = -\lambda_{2,t} - \lambda_{3,t} + \lambda_{7,t}\frac{\gamma_s \mu}{q_t} = 0 \tag{G.62}$$

$$\frac{\partial \mathcal{L}}{\partial D_{2,t}} = \lambda_{2,t}\theta(1 - v_t)s_t - \lambda_{4,t} - \lambda_{5,t}\theta W_t - \lambda_{6,t}\theta Z_t + \lambda_{7,t}[\gamma_w \theta W_t + \gamma_z \theta Z_t] = 0 \tag{G.63}$$

$$\begin{aligned}\frac{\partial \mathcal{L}}{\partial W_{t+1}} &= \lambda_{4,t+1} - \lambda_{5,t} + \lambda_{5,t+1}[1 - \delta_w - \varepsilon_w - \theta(D_{2,t+1} + (1 - v_{t+1})S_{t+1})] \\ &\quad +\lambda_{7,t+1}[\phi_w \varepsilon_w + \gamma_w \theta D_{2,t}] = 0\end{aligned} \tag{G.64}$$

$$\begin{aligned}\frac{\partial \mathcal{L}}{\partial Z_{t+1}} &= \lambda_{4,t+1} - \lambda_{6,t} + \lambda_{6,t+1}[1 - \delta_z - \varepsilon_z - \theta(D_{2,t+1} + (1 - v_{t+1})S_{t+1})] \\ &\quad +\lambda_{7,t+1}[\phi_z \varepsilon_z + \gamma_z \theta D_{2,t}] = 0\end{aligned} \tag{G.65}$$

$$\frac{\partial \mathcal{L}}{\partial F_{1,t+1}} = \lambda_{4,t+1}(1 + \Gamma) - \lambda_{7,t} + \lambda_{7,t+1}(1 - \delta_f) = 0 \tag{G.66}$$

APPENDIX H: COMPUTER CODE

To perform the numerical simulations, the model is reformulated as a non-linear programming (NLP) problem. Specifically, the simulations cover the period from 2023 to 2272, providing a 250 year planning horizon, with results generated at an annual frequency. The last 50 years are discarded, and only the horizon 2023 to 2222 is considered, in order to eliminate distortions arising from the finite-horizon terminal condition. The model is implemented and solved using GAMS with the CONOPT4 algorithm. As highlighted by Cai (2019), GAMS offers greater flexibility compared to MATLAB, and CONOPT4 is recognized as a more robust and efficient solver for non-linear programming problems than MATLAB's *fmincon* algorithm.

To ensure robustness, the model is also solved in MATLAB using the CasADi framework (Andersson et al., 2019). For context, the DICE (Dynamic Integrated Climate-Economy) model, originally developed by Nordhaus (1992, 1993), remains the most influential integrated assessment model (IAM) in the literature. Nordhaus's DICE model was initially designed and implemented in GAMS, but alternative implementations have emerged over time. For instance, Kellett et al. (2016) developed MATLAB code to solve DICE2013R and DICE2016R using CasADi, while Lemoine (2020) introduced a solution method for DICE2016R using the KNITRO solver.

The baseline GAMS file is named *DISE_2024_01.gms*. Results are saved in Excel files. Figures in the manuscript are produced in MATLAB, using the script *Figures01.m*, which is executed after *DISE_2024_01.gms* have been run in GAMS and the results stored in Excel files. Codes for replication can be found at Harvard Dataverse (https://doi.org/10.7910/DVN/I1AHM2).

There is also a version of DISE-2024 in MATLAB. The files are *dise_ocp.m* as the main script, *Space1999.m* containing the initial values and the calibration, and the function file *ocp.m* for the computational algorithm. To run this MATLAB version, it is necessary to have CasADi (Andersson et al., 2019) installed.

Finally, there is a companion app for a full sensitivity analysis of DISE-2024. This is a GAMS MIRO app, which allows users to solve the model using the GAMS engine and perform a comprehensive sensitivity analysis on the model's key parameters. This app can be found at https://miro.gams.com/gallery/app_direct/dise_2024/.

References

[1] Adilov, N., Alexander, P., Cunningham B. and Albertson, N. (2022). An analysis of launch cost reductions for low Earth orbit satellites. *Economics Bulletin*, 42(3): 1561-1574.

[2] Ackerman, F., Stanton, E. A. and Bueno, R. (2013). Epstein-Zin utility in DICE: Is risk aversion irrelevant to climate policy? *Environmental and Resource Economics*, 56: 73-84.

[3] Andersson, J. A. E., Gillis, J., Horn, G., Rawlings, J. B. and Diehl, M. (2019). CasADi – A software framework for nonlinear optimization and optimal control. *Mathematical Programming Computation*, 11(1): 1-36.

[4] Anz-Meador, H., Opiela, H. and Liou, J. C. (2022). History of On-orbit Satellite Fragmentations, 16th Edition Orbital Debris Program Office, NASA.

[5] Australian Space Weather Agency. 1999. *Satellite orbital decay calculations.* Sidney: Australia.

[6] Barsky, R. B., Juster, F. T., Kimball, M. S. and Shapiro, M. D. (1977). Preference Parameters and Behavioral Heterogeneity: An Experimental Approach in the Health and Retirement Study. *The Quarterly Journal of Economics*, 112(2): 537-579.

[7] Barro, R. J. (2015). Environmental Protection, Rare Disasters and Discount Rates. *Economica*, 82(325): 1-23.

[8] Bongers, A. and Torres, J. L. (2023). Orbital debris and the market for satellites. *Ecological Economics*, 209: 107831.

[9] Bongers, A. and Torres, J. L. (2024). Star Wars: Anti-satellite weapons and orbital debris. *Defence and Peace Economics*, 35(7): 826-845.

[10] Bongers, A., Ortiz, C. and Torres, J. L. (2025). DISE: A dynamic integrated space-economy model for the evaluation of debris mitigation policies. *Environmental and Resource Economics*, 88, 2125-2156.

[11] Böhringer, C., Löchel, A. and Rutherford, T. F. (2007). Decomposing the integrated assessment of climate change. *Journal of Economic Dynamics and Control*, 31(2): 683-702.

[12] Bryce.(2020). Smallsats by the numbers 2020 Bryce Space and Technology.

[13] Bureau of Economic Analysis (2023). *Space Economy Data, 2012-2021.*

[14] Byers, M. and Boley, A. (2023). *Who Owns Outer Space? International Law, Astrophysics and the Sustainable Development of Space*. Cambridge University Press.

[15] Cai, Y. (2019). Computational methods in environmental and resource economics. *Annual Review of Resource Economics*, 11: 59-82.

[16] Chakravarty, S. (1962). The existence of an optimum savings program. *Econometrica*, 30(1): 178-187.

[17] Chetty, R. (2006). A new method of estimating risk aversion. *American Economic Review*, 96(5): 1821–1834.

[18] Cook, G. E. (1965). Satellite drag coefficients. *Planetary and Space Science*, 13(10): 929-946.

[19] Cordelli, A., Farinella, P., Anselmo, L., Pardini, C. and Rossi, A. (1993). Future collisional evolution of Earth-orbiting debris. *Advances in Space Research*, 13(8): 215-219.

[20] Corrado, L., Grassi, S., Paolillo, A. and Silgado, E. (2023). The macroeconomic spillovers from space activity. *PNAS*, 120(43), e2221342120.

[21] D'Ambrosio, A., Lifson, M. and Linares, R. (2022). The capacity of low Earth orbit computed using source-sink modeling [Internet], viewed 2022 Aug 28, available from: https://arxiv.org/ abs/2206.05345

[22] Dasgupta, P. (2008). Discounting climate change. *Journal of risk and uncertainty*, 37: 141–169.

[23] Doornbos, E., Bruinsma, S., Fritsche, B., Visser, P., van den Ijssel, J., da Encarnação, J. and Kern, M. (2013). Air density and wind retrieval using GOCE data. *ESA Living Planet*.

[24] Evans, D. J. (2005). The elasticity of marginal utility of consumption: Estimates for 20 OECD countries. *Fiscal Studies*, 26(2): 197–224.

[25] Epstein, L. G. and Zin, S. E. (1989). Substitution, risk aversion, and the temporal behavior of consumption and asset returns: A theoretical framework. *Econometrica*, 57(4): 937-969.

[26] Farinella, P. and Cordelli, A. (1991). The proliferation of orbiting fragments: a simple mathematical model. *Science and GlobalSecurity*, 2: 365-378.

[27] Feenstra, R. C., Inklaar, R. and Timmer, M. P. (2015). The Next Generation of the Penn World Table. *American Economic Review*, 105(10): 3150-3182.

[28] Fraumeni, B.M. (1997). The Measurement of Depreciation in the U.S. National Income and Product Accounts. *Survey of current business*, 7-23.

[29] Gallois, P. (1987). Life expectancy of communication satellites, *Electronics and Power* 33 (9): 547-550.

[30] Greenwood, J., Hercowitz, Z. and Krusell, P. (1997). Long-Run Implications of Investment-Specific Technological Change. *American Economic Review*, 87(3): 342–362.

[31] Gupta, S., Kangur, A., Papageorgiou, C. and Wane, A.(2014). Efficiency-adjusted public capital and growth.*World Development*, 57:164–178.

[32] Guyot, J. (2024). Economic analysis of Earth orbital exploitation.

[33] Guyot, J. and Rouillon, S. (2023). Sustainable management of space activity in low Earth orbit. *Journal of Environmental Economics and Policy*, 13(2): 188-212.

[34] Guyot, J. and Rouillon, S. (2024). Sustainable management of space activity in low Earth orbit. *Journal of Environmental Economics and Policy*, 13(2): 188-212.

[35] Hansen, L. P. and Singleton, K. J. (1982). Generalized Instrumental Variables Estimation of Nonlinear Rational Expectations Models. *Econometrica*, 50(5): 1269-1286.

[36] Hassell, M. P. (1975). Density-dependence in single-species populations. *British Ecological Society*, 44(1): 283-295.

[37] Jacchia, L. (1972). Atmospheric models in the region from 110 to 2000 km. In CIRA 1972: COSPAR International Reference Atmosphere, 227–338.

[38] Jiang, Y. (2020). Debris cloud of India anti-satellite test to Microsat-R satellite. *Heliyon*, 6(8): 1-6.

[39] Johnson, N.L., Krisko, P.H., Liou, J.C. and Anz-Meador, P.D. (2001). NASA's new breakup model of evolve 4.0. *Advances in Space Research*, 28(9): 1377–1384.

[40] Kawamoto, S., N. Nagaoka, T. Sato, and T. Hanada. 2019. "Impact on Collision Probability by Post Mission Disposal and Active Debris Removal." First International Orbital Debris Conference.

[41] Kellett, C. M., Faulwasser, T. and Weller, S. R. (2016). DICE2013R-mc: A Matlab/-CasADi implementation of vanilla DICE2013R. arXiv:1608.04294.

[42] Kendrick, D. and Taylor, L. (1970). Numerical solution of nonlinear planning models. *Econometrica*, 38(3): 453-467.

[43] Kessler, D. J. and B. G. Cour-Palais. 1978. "Collision frequency of artificial satellites: The creation of a debris belt." *Journal of Geophysical Research* 83 (A6): 2637-2646.

[44] Kessler, D. J., Johnson, N. L., Liou, J. C. and Matney, M. (2010). The Kessler syndrome: Implications to future space operations. AAS-10-016.

[45] King-Hele, D. G. (1987). *Satellite orbits in an atmosphere: theory and application*. Springer Netherlands.

[46] Krag, H., M. Serrano, V. Braun, P. Kuchynka, M. Catania, J. Simiski, M. Schimmerohn, X. Marc, D. Kujiper, I. Shurmer, A. O'Connell, M. Otten, I. Muñoz, J. Morales, M. Wermuth and D. McKissock. 2017. A 1 cm space debris impact onto the Sentinel-1A solar array. *Acta Astronautica* 137: 434-443.

[47] Krisko, P.H. (2007). The predicted growth of the low-Earth orbit space debris environment - An assessment of future risk for spacecraft. *Journal of Aerospace Engineering*, 221(6): 975-985.

[48] Krisko, P.H., Johnson, N.L. and Opiela, J.N. (2001). EVOLVE 4.0 orbital debris mitigation studies. *Advances in Space Research*, 28(9): 1385-1390.

[49] Lafleur, J.L. (2011). Extension of a simple mathematical model for orbital debris proliferation and mitigation. *American Astronautical Society*, 11-173.

[50] Lau, M. I., Pahlke, A. and Rutherford, T. F. (2002). Approximating infinity-horizon models in a complementarity format: A primer in dynamic general equilibrium analysis. *Journal of Economic Dynamics and Control*, 26(4): 577-609.

[51] Lemoine, D. (2020). Incentivizing Negative Emissions Through Carbon Shares. University of Arizona Working Paper 20-08.

[52] Letizia, F., C. Colombo, H. G. Lewis, and H. Krag. (2017). Extending the ECOB space debris index with fragmentation risk estimation. Proc. 7th European Conference on Space Debris, Darmstadt, Germany, 18–21 April 2017, published by the ESA Space Debris Office.

[53] Lewis, H.G. (2020). Understanding long-term orbital debris population dynamics. *Journal of Space Safety Engineering*, 7: 164-170.

[54] Lewis, H.G., Swinerd, G.G., Newland, R.J. and Saunders, A. (2009). The fast debris evolution model. *Advances in Space Research*, 44: 568-578.

[55] Lifson, M., D'Ambrosio, A., Arnas, D. and Linares, R. (2022). How many satellites can we fit in low Earth orbit?: Capacity integrating Risk-based and Intrinsic Methods. AAS/AIAA Astrodynamics Specialist Conference

[56] Liou, J.C., Hall, D.T., Krisko, P.H. and Opiela, J.N. (2004). LEGEND - a three-dimensional LEO-to-GEO debris evolutionary model. *Advances in Space Research*, 34: 981-986.

[57] Locke, J., Colvin, T. J., Ratliff, L., Abdul-Hamid, A. and Samples, C. (2024). *Cost and benefit analysis of mitigating, tracking, and remediating orbital debris*. Office of Technology, Policy, and Strategy. NASA.

[58] Mains, D. L. and Sorge, M. E. (2022). The IMPACT satellite fragmentation model. *Acta Astronautica*, 195: 547-555.

[59] Mains, D. L., Peterson, G. E., McVey, J. P., Maldonado, J. C. and Sorge, M. E. (2024). Forensic analysis of recent debris-generating events. *Journal of Space Safety Engineering*, 11: 388-394.

[60] Mehra, R. and Prescott, E. C. (1985). The equity premium: A puzzle. *Journal of Monetary Economics*, 15(2): 145-161.

[61] Metha, P. M., Smriti, N. P., Crip, N. H., Sheridan, P. L., Siemes, C., Marchet, G. and Bruinsma, S. (2022). Satellite drag coefficient modeling for Thermosphere science and mission operations. *Advances in Space Research*, 72(12): 5443-5459.

[62] McDowell, J. (2019). *Space Activities 2018*. Jonathan's Space Report.

[63] McDowell, J. (2020). *Space Activities 2019*. Jonathan's Space Report.

[64] McDowell, J. (2023). *Space Activities 2022*. Jonathan's Space Report.

[65] McDowell, J. (2024). *Space Activities 2023*. Jonathan's Space Report.

[66] McKnight, D., Witner, R., Letizia, F., Lemmens, S., Anselmo, L., Pardini, C., Rossi, A., Kunstadter, C., Kawamoto, S., Aslanov. V., Dolado-Pérez, J. C., Ruch, V., Lewis, H., Nicolls, M., Jing, L., Dan, S., Dongfang, W., Baranov, A. and Grishko, D. (2021). Identifying the 50 statistically-most-concerning derelict objects in LEO. *Acta Astronautica*, 181: 282-291.

[67] NASA (2007). Detection of debris from Chinese ASAT test increases; One minor fragmentation event in second quarter of 2007. *Orbital Debris Quarterly Review* 11(3): 1-2.

[68] NASA (2011). Fiftieth anniversary of first on-orbit satellite fragmentation. *Orbital Debris Quarterly News*, 15(3): 3-5.

[69] NASA (2020). The tracked objects in Low Earth Orbit: 2000–2020. *Orbital Debris Quarterly Review* 24(4): 11.

[70] NASA (2022). International Space Station Maneuvers to Avoid Another Russian ASAT Fragment. *Orbital Debris Quarterly Review*, 26(4): 1-14.

[71] NASA (2024). Monthly number of tracked objects in Earth orbit by object type. *Orbital Debris Quarterly Review*, 28(3): 10-11.

[72] Niccolai, L. and Mengali, G. (2024). Decay time estimate for LEO spacecraft. *Acta Astronautica*, 225: 601-614.

[73] Nozawa, W., Kurita, K., Tamaki, T. and Managi, S. (2023). To what extent will space debris impact the economy? *Space Policy*, 66: 101580.

[74] OECD (2020). Space sustainability: The economics of space debris in perspective. OECD Science, Technology and Industry Policy Papers n. 87.

[75] Pardini, C. and Anselmo, L. (2014). Review of past on-orbit collisions among cataloged objects and examination of the catastrophic fragmentation concept. *Acta Astronautica*, 100: 30-39.

[76] Percy, T. (2015). *Simplified population growth modelling for low earth orbit*. Dissertations, 76. University of Alabama.

[77] Pfrang, K., and Weeden, B. (2020b). Indian Direct Ascent Anti-Satellite Testing. Secure World Foundation. August. Promoting Cooperative Solutions for Space Sustainability | Secure World (swfound.org)

[78] Prieto, D. M., Graziano, B. P. and Robers, P. C. E. (2014). Space drag modelling. *Progress in Aerospace Sciences*, 64(1): 56-65.

[79] Ramsey, F. P. (1928). A mathematical theory of saving. *Economic Journal*, 38(152): 543-559.

[80] Rao, A., Moretto, M., Holzinger, M., Kaffine, D. and Weeden, B. (2023). OPUS: An integrated model for satellites and orbital debris. arXiv preprint 2309.10252v.

[81] Rao and Letizia (2022). An integrated debris environment assessment model. arXiv preprint 2205.05205.

[82] Rossi, A., Cordelli, A., Farinella, P. and Anselmo, L. (1994). Collisional evolution of the Earth's orbital debris cloud. *Journal of Geophysical Research*, 99(E11): 23195-23210.

[83] Rutherford, T. F. (1995). Extension of GAMS for complementarity problems arising in applied economic analysis. *Journal of Economic Dynamics and Control*, 19: 1299-1324.

[84] Satellite Industry Association (2023). *SIA Reports Record Growth for the Satellite Industry in 2023*.

[85] Space Foundation (2023). *The Space Report 2023 Q2*.

[86] Stern, N. (2006). *The economics of climate change: The Stern Review*, Cambridge University Press.

[87] Szpiro, G. (1986). Measuring risk aversion: An alternative approach. *Review of Economics and Statistics*, 68(1): 156-159.

[88] Rossi, A. and Farinella, P. (1998). Earth-Orbiting Debris Cloud and Its Collisional Evolution. In: Benest, D., Froeschlé, C. (eds) Impacts on Earth. Lecture Notes in Physics, vol 505. Springer, Berlin, Heidelberg.

[89] Talent, D. (1992). Analytical model for orbital debris environmental management. *Journal of Spacecraft Rocket*, 29(4): 508-551.

[90] United Nations (2024). *World Population Prospects 2024*. Population Division, Department of Economics and Social Affairs, United Nations.

[91] Wang, X. W. and Liu, J. (2019). An introduction to a new space debris evolution model: SOLEM. *Advances in Astronomy*, 2019: 2738276.

[92] Weeden, B. (2020a). Chinese Direct Ascent Anti-Satellite Testing. Secure World Foundation. August. Promoting Cooperative Solutions for Space Sustainability | Secure World (swfound.org)

[93] Weeden, B. 2020b. X-37B Orbital Test Vehicle Fact sheet. Secure World Foundation. May. Promoting Cooperative Solutions for Space Sustainability | Secure World (Swfound.Org)

[94] Weitzman, M. L. (2007). A review of the Stern Review on the economics of climate change. *Journal of Economic Literature*, 45: 703–724.

[95] Wright, E., Boley, A. and Byers, M. (2024). Improving casualty risk estimates for uncontrolled rocket body reentries. *Journal of Space Safety Engineering*, 11(1): 74-79. [ ]